MULTISLICE SIMULATION OF TEM IMAGES

by

Graham D. Reid

Thesis

submitted in partial fulfillment of

the requirements of the Degree of

Bachelor of Science with Honours in

Physics.

Acadia University

May 2012

© Graham Reid, 2012

This thesis by Graham Reid

is accepted in its present form by the

Department of Physics

as satisfying the thesis requirements for the Degree of

Bachelor of Science with Honours.

Approved by the Thesis Supervisors

Michael Robertson Date

Approved by the Head of the Department

Dr. J. Craig Bennett Date

Approved by the Honours Committee

Date

I, Graham Reid, hereby grant permission to the University Librarian at Acadia University to provide copies of the thesis, on request, on a non-profit basis.

Signature of Author

Date

Acknowledgements

First of all I would like to thank my family and friends who have supported me throughout my life. I would like to give special thanks to Michael Robertson and Anthony Tong who supported my summer research at Acadia and taught me a great deal. Finally I would like to acknowledge NSERC's generous funding of my research.

Table of Contents

Acknowledgements vii

Table of Contents ix

List of Figures xi

Abstract xiii

Chapter 1. Introduction 1
- 1.1 Motivation 1
- 1.2 Thesis Structure 2

Chapter 2. Derivations 5
- 2.1 Approximating the Schrödinger Equation 5
- 2.2 Multislice Derivation 8
- 2.3 Second Derivative Multislice Derivation 15
- 2.4 Wave Solution Derivation 17
- 2.5 Finite Difference Approximations 20

Chapter 3. Stability Analysis 23
- 3.1 Background 23
- 3.2 Multislice 25
- 3.3 Second Derivative Multislice 28
- 3.4 Wave Solution 29
- 3.5 Finite Difference Approximations 30

Chapter 4. Atomic Potentials 31
- 4.1 The Born Approximation 31
- 4.2 Parameterization of Electron Scattering Factors 34
- 4.3 Comparison of Electron Scattering Factors 37
- 4.4 Comparison of Atomic Potentials 39

Chapter 5. Comparison of Methods 41
- 5.1 Conditions and Methodology 41
- 5.2 Thermal Variation 44
- 5.3 Kirkland versus Peng Parameterization 46
- 5.4 Unbounded Potentials versus Bounded Potentials 50
- 5.5 Multislice versus RK4 58
- 5.6 Effects of super cell Size 61

Chapter 6. Conclusions 67
- 6.1 Summary of Results 67
- 6.2 Recommendations for Future Work 68

Appendix A. Simulation Conditions **69**

Bibliography **75**

List of Figures

2.1 Relative magnitudes of the first derivative term and second derivative term taken from a point directly above a [100] gold atomic column with the atoms located at the principle peaks 8

4.1 Comparison of potential calculation methods 35
4.2 Kirkland and Peng electron scattering factors for gold plotted against the magnitude of the scattering vector 37
4.3 Kirkland and Peng electron scattering factors for silicon plotted against the magnitude of the scattering vector. 38
4.4 Kirkland (Gaussian and Lorentzian) and Peng (Gaussian) parameterizations of atomic potentials for gold plotted as a function of distance from the center of the atom 39
4.5 Kirkland (Gaussian and Lorentzian) and Peng (Gaussian) parameterizations of atomic potentials for silicon plotted as a function of distance from the center of the atom 40

5.1 a) CBED pattern and b) corresponding graph of the radially integrated intensities for 50 nm of [111] silicon at 300 KeV using CM30 simulation conditions 43
5.2 Radially integrated intensity of four identical simulations of [111] silicon at 300 KeV using the unbounded potential formulation 44
5.3 Radially integrated intensity of two simulations of [111] silicon at 100 KeV using bounded potential formulation for both the Peng and Kirkland potentials 46
5.4 Radially integrated intensity of two simulations of [111] silicon at 100 KeV using bounded potential formulation for both the Peng and Kirkland potentials 47
5.5 Radially integrated intensity of two simulations of [111] silicon at 100 KeV using bounded potential formulation for both the Peng and Kirkland potentials 47
5.6 Radially integrated intensity of two simulations of [111] silicon at 300 KeV using bounded potential formulation for both the Peng and Kirkland potentials 48
5.7 Radially integrated intensity of two simulations of [111] silicon at 300 KeV using bounded potential formulation for both the Peng and Kirkland potentials 48
5.8 Radially integrated intensity of two simulations of [111] silicon at 300 KeV using bounded potential formulation for both the Peng and Kirkland potentials 49
5.9 Radially integrated intensity of three simulations of [111] silicon at 100 KeV using the bounded potential formulation 50
5.10 Radially integrated intensity of three simulations of [111] silicon at 300 KeV using the bounded potential formulation 51
5.11 Radially integrated intensity of [111] silicon at 300 KeV for both the bounded and unbounded potential formulations 52
5.12 Radially integrated intensity of [111] silicon at 300 KeV for both the bounded and unbounded potential formulations 52
5.13 Radially integrated intensity of [111] silicon at 300 KeV for both the bounded and unbounded potential formulations 53
5.14 Radially integrated intensity of [111] silicon at 300 KeV for both the bounded and unbounded potential formulations 53
5.15 Radially integrated intensity of [111] silicon at 300 KeV for both the bounded and unbounded potential formulations with no thermal effects 54

5.16 Radially integrated intensity of [111] silicon at 300 KeV for both the bounded and unbounded potential formulations with no thermal effects 54
5.17 Radially integrated intensity of [111] silicon at 300 KeV for both the bounded and unbounded potential formulations with no thermal effects 55
5.18 Radially integrated intensity of [111] silicon at 300 KeV for both the bounded and unbounded potential formulations 55
5.19 Radially integrated intensity of [111] silicon at 300 KeV for the bounded potential formulation with $\Delta z = 0.1161$ Å and unbounded potential formulations 56
5.20 Coefficient of variance between bounded potential formulation with $\Delta z = 0.1161$ Å and unbounded potential formulations 57
5.21 Runge-Kutta, bounded multislice and unbounded multislice simulations of 300 KeV [111] silicon for $\Delta z = 0.003135$ Å. 58
5.22 Runge-Kutta, bounded multislice and unbounded multislice simulations of 300 KeV [111] silicon for $\Delta z = 0.003135$ Å. 59
5.23 Runge-Kutta simulations of 300 KeV [111] silicon for $\Delta z = 0.003135$ Å and $\Delta z = 0.0003135$ Å 60
5.24 Equivalence of periodic boundry conditions and tiling finite size initial conditions throughout all space 61
5.25 Radially integrated CBED intensity plotted as a function of radius for various super cell sizes 62
5.26 Radially integrated real space intensity plotted as a function of radius for various super cell sizes 63
5.27 Total radially integrated real space intensity plotted as a function of radius for various super cell sizes 64

Abstract

Numeric simulation of physical processes can be a highly useful tool that enables experimenters to investigate situations and processes that would otherwise be difficult or impossible to examine in the lab. Applied to the subject of electron diffraction and the simulation of transmission electron microscope images, numerical methods enable experimenters to examine the effects of defects in materials and help to identify imaging artifacts [4].

In this thesis, two important aspects of image simulation, specimen potential and calculation methodology have been investigated. An alternative and more accurate method of calculating the specimen potential is investigated and two variants on the multislice method (originally developed by Cowley and Moodie [2]) for transmission electron microscope image simulation are presented and analyzed. Additionally, a brief overview of the effects of super-cell size on real space and reciprocal space images is given.

It is shown that the standard method of calculating the specimen potential gives results consistent with the new potential calculation method when the simulation slice thickness is made small. This observation indicates that Kirkland's minimum slice thickness hypothesis may be in error [4]. In addition, it is demonstrated that the multislice method is not convergent on a direct numeric integration of the Schrödinger equation and that the dimensions of the simulated super cell contribute significantly to image formation.

Chapter 1

Introduction

1.1 Motivation

Numeric simulation of physical processes can be a highly useful tool that enables experimenters to investigate situations and processes that would otherwise be difficult or impossible to examine in the lab. Applied to the subject of electron diffraction and the simulation of transmission electron microscope (TEM) images, numerical methods enable experimenters to examine the effects of defects in materials and help to identify imaging artifacts [4]. Numerical methods help experimenters identify the best equipment and conditions for the task at hand by minimizing the trial and error process while facilitating the interpretation of experiments [4].

Inherently, the utility of a simulation tool is limited by its accuracy; if a numerical method gives results that differ substantially from the correct result, its applicability is limited and conclusions drawn from it may be erroneous. Specifically, for the case of TEM diffraction patterns presented in this thesis, two important aspects of image simulation, specimen potential and calculation methodology have been investigated. An alternative and more accurate method of calculating the specimen potential is investigated, and two variants on the multislice method (originally developed by Cowley and Moodie [2]) for TEM image simulation are presented and analyzed.

1.2 Thesis Structure

The topic of this thesis is the simulation of Convergent Beam Electron Diffraction (CBED) patterns using various modification of the standard multislice method to improve accuracy. A background knowledge of crystallography, electron microscope operation and diffraction pattern analysis is assumed. The focus is on the numerical methods themselves and the results of the simulations.

Chapter 2 presents an in-depth derivation of the standard multislice method closely following the conventions and derivation presented in Kirkland [4]. Following the derivation of the standard multislice method two new multislice methods, which attempt to include the contribution from a term neglected in the standard multislice solution, are derived. In addition, a brief derivation of a finite difference method and a Runge-Kutta method are given.

In Chapter 3, the numerical stability of the methods presented in Chapter 2 are explored using a form of Fourier stability analysis. It is shown that the standard multislice solution and wave solution are unconditionally stable while the second derivative multislice solution is unstable. This demonstrates the utility of both the standard multislice solution and wave solution while indicating that the second derivative multislice solution is unsuitable for implementation.

The subject of Chapter 4 is the calculation of the specimen potentials and the relationship between atomic scattering factors and atomic potentials. An alternative method of calculating the projected atomic potential (a quantity used by all of the methods introduced in Chapter 2) is presented.

The potential calculation methods introduced in Chapter 4 are investigated in Chapter 5 and it is demonstrated that the standard multislice solution with unbounded potentials is accurate to much smaller slice thicknesses than indicated by Kirkland. The results of the multislice simulations are then compared to a series of Runge-Kutta simulations and it is shown that the two methods give substantially different results. Additionally, it is shown that there are substantial variations between thickly and thinly sliced simulations and that the the size of the super-cell used in the simulation can have a significant effect on both the real space and reciprocal space images.

Finally, in Chapter 6, the findings are summarized and conclusions and recommendations for future work are discussed.

Chapter 2

Derivations

This chapter is divided into four sections detailing the derivation of the Schrödinger equation for fast electrons as presented in [4] and the derivation of three multislice methods to solve this equation. For the purposes of this thesis, the multislice method presented by Kirkland [4] and derived in section 2.2 is referred to as the "standard multislice solution" while the additional methods derived in sections 2.3 and 2.4 are referred to as the "second derivative multislice solution" and the "wave solution", respectively.

2.1 Approximating the Schrödinger Equation

The Schrödinger equation for an electron of mass m, charge e and kinetic energy E moving in an electrostatic field V is written as:

$$\left[\frac{\hbar^2}{2m}\nabla^2 - eV\left(x,y,z\right)\right]\psi_f\left(x,y,z\right) = E\psi_f\left(x,y,z\right) \tag{2.1}$$

where $\psi_f\left(x,y,z\right)$ is the electron wave function.

In addition to the electrostatic field encountered by an electron traveling through the specimen in a TEM, the electron will also interact with the magnetic field of the objective lens. According to Kirkland, the action of the objective lens magnetic field is negligible on the scale of the specimen thickness [4].

In an electron microscope, the energy of the imaging electrons ($>$100 keV) is large compared to the energy gained or lost by these electrons within the sample. If the electron motion is aligned initially along the z axis, is it possible to treat the interaction with the specimen as a relatively minor perturbation [4]. In order to remove the rapidly varying part of the solution due to the short wavelength of the electrons, the wave function is factored into a plane wave traveling along the z axis and another function which varies more slowly in z and captures the motion of the electron due its interaction with the specimen.

$$\psi_f\left(x,y,z\right) = \psi\left(x,y,z\right)\exp\left(2\pi iz/\lambda\right) \tag{2.2}$$

For the sake of conciseness, $\psi\left(x,y,z\right)$ will be replaced with ψ in subsequent equations. When a term such as $\psi\left(z+\Delta z\right)$ appears in an equation, it is shorthand for $\psi\left(x,y,z+\Delta z\right)$.

It is assumed that only elastic scattering processes are involved, so the total kinetic energy of the electron is:

$$E = \frac{h^2}{2m\lambda^2} \tag{2.3}$$

where m and λ are the relativistic mass and wavelength, respectively. Applying the ∇^2 operator to equation 2.2, results in:

$$\begin{aligned}
\nabla^2\psi_f &= \nabla^2\psi\exp\left(2\pi iz/\lambda\right)\\
&= \left[\nabla^2_{xy}+\frac{\partial^2}{\partial z^2}\right]\psi\exp\left(2\pi iz/\lambda\right)\\
&= \nabla^2_{xy}\left[\psi\exp\left(2\pi iz/\lambda\right)\right]+\frac{\partial^2}{\partial z^2}\left[\psi\exp\left(2\pi iz/\lambda\right)\right]\\
&= \exp\left(2\pi iz/\lambda\right)\left[\nabla^2_{xy}\psi+\frac{\partial^2\psi}{\partial z^2}+\frac{4\pi i}{\lambda}\frac{\partial\psi}{\partial z}-\frac{4\pi^2}{\lambda^2}\right] \qquad (2.4)
\end{aligned}$$

Substituting equations 2.4 and 2.3 into equation 2.1 gives,

$$\frac{-\hbar^2}{2m}\exp\left(2\pi iz/\lambda\right)\left[\nabla^2_{xy}\psi+\frac{\partial^2\psi}{\partial z^2}+\frac{4\pi i}{\lambda}\frac{\partial\psi}{\partial z}\right]-eV\psi\exp\left(2\pi iz/\lambda\right)=0 \tag{2.5}$$

and simplifying equation 2.5, the Schrödinger equation for fast electrons is obtained:

$$\left[\nabla_{xy}^2 + \frac{\partial^2}{\partial z^2} + \frac{4\pi i}{\lambda}\frac{\partial}{\partial z} + \frac{2meV}{\hbar^2}\right]\psi = 0 \tag{2.6}$$

2.2 Multislice Derivation

The standard multislice solution neglects the $\frac{\partial^2\psi}{\partial z^2}$ term in equation 2.6 given that $\left\|\frac{\partial^2\psi}{\partial z^2}\right\| \ll \left\|\frac{4\pi i}{\lambda}\frac{\partial\psi}{\partial z}\right\|$. The validity of this approximation has been tested and plotted in Figure 2.1 for the case of [100] oriented gold. The multislice formalism presented in Kirkland is therefore a solution to equation 2.7:

$$\left[\nabla^2_{xy} + \frac{4\pi i}{\lambda}\frac{\partial}{\partial z} + \frac{2meV}{\hbar^2}\right]\psi = 0 \tag{2.7}$$

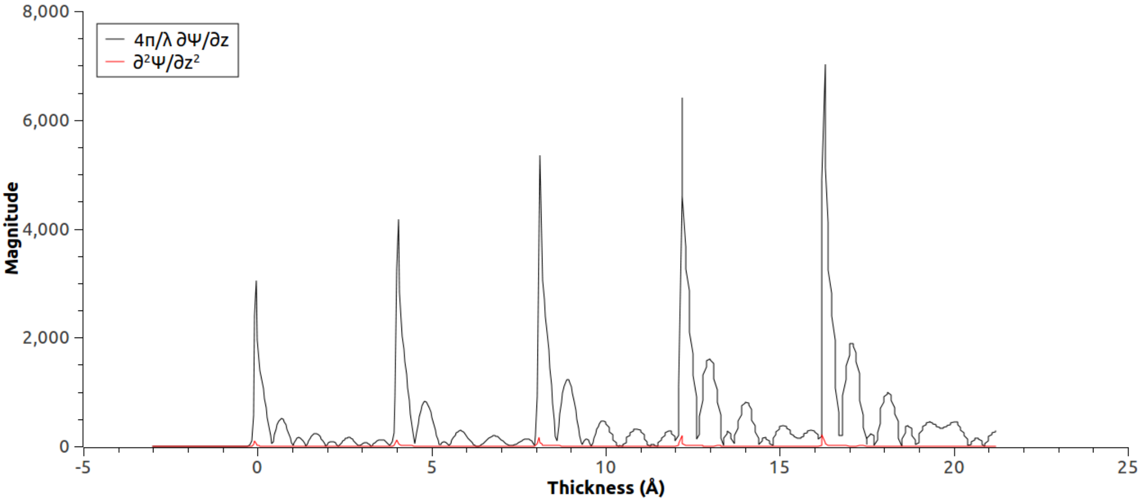

Figure 2.1: The relative magnitudes of the first and second derivative terms taken from a point directly above a [100] gold atomic column with the atoms located at the principle peaks. As gold is a heavy nuclei, the scattering should be more pronounced than for lighter atoms leading to a significant second derivative term. It should be noted that this figure is only approximately correct as the data was calculated from a form of the multislice solution which neglects the second derivative term.

Although the full derivation of the multislice solution is presented in [4], an expanded derivation is presented below for completeness as well as to provide the background for the derivations presented in sections 2.3 and 2.4.

Rearrange equation 2.7 for $\frac{\partial\psi}{\partial z}$,

$$\frac{\partial\psi}{\partial z} = \frac{\lambda i}{4\pi}\nabla^2_{xy}\psi + \frac{2meV\lambda i}{4\pi\hbar^2}\psi \tag{2.8}$$

collecting variables, $\sigma = \frac{me\lambda}{2\pi\hbar^2}$, and substituting into equation 2.8 leads to:

$$\frac{\partial\psi}{\partial z} = \frac{\lambda i}{4\pi}\nabla^2_{xy}\psi + i\sigma V\psi \tag{2.9}$$

Using a finite difference approximation to evaluate equation 2.9 would lead to an algorithm that is essentially Euler's method; it would require excessively small step sizes to remain accurate and would likely suffer from frequency degradation as certain spatial frequencies were promoted or deteriorated unequally [4]. If the solution is cast into an exponential form with a mostly imaginary argument, the norm of the function will be preserved [4]. Hence, we approximate ψ by a Taylor series expansion in Δz:

$$\begin{aligned}\psi\left(z+\Delta z\right) &= \psi + \Delta z\frac{\partial}{\partial z}\psi + \frac{\Delta z^2}{2}\frac{\partial^2}{\partial z^2}\psi + \cdots \\ &= \psi + \Delta z\frac{\partial}{\partial z}\psi + O\left(\Delta z^2\right)\end{aligned} \tag{2.10}$$

Substituting 2.9 into 2.10, the wave function at $z + \Delta z$ is given by:

$$\begin{aligned}\psi\left(z+\Delta z\right) &= \psi + \Delta z\left[\frac{\lambda i}{4\pi}\nabla^2_{xy}\psi + i\sigma V\psi\right] + O\left(\Delta z^2\right) \\ &= \left[1 + \Delta z\left(\frac{\lambda i}{4\pi}\nabla^2_{xy} + i\sigma V\right)\right]\psi + O\left(\Delta z^2\right)\end{aligned} \tag{2.11}$$

Comparing equation 2.11 with the Taylor series expansion of $\exp x$,

$$e^x = 1 + x + \frac{1}{2!}x^2 + \frac{1}{3!}x^3 + \cdots \tag{2.12}$$

$$\approx 1 + x + O\left(x^2\right) \tag{2.13}$$

the two equations are identical to second order in Δz. Thus, to second order in Δz, equation 2.11 may be expressed as:

$$\psi\left(z+\Delta z\right)=\exp\left[\Delta z\frac{\lambda i}{4\pi}\nabla_{xy}^{2}+i\sigma V\Delta z\right]\psi+O\left(\Delta z^{2}\right) \tag{2.14}$$

In the previous equation, $V\left(x,y,z\right)\Delta z$ is not a physically accurate parameter as it represents the projected atomic potential to only first order accuracy. A more physically realistic picture can be achieved by replacing $V\left(x,y,z\right)\Delta z$ with $\bar{V}=\int_{z}^{z+\Delta z}V\left(x,y,z_{2}\right)dz_{2}$ $=V\left(x,y,z\right)\Delta z+O\left(\Delta z^{2}\right)$. Although this substitution appears to introduce an additional second order error term, it ensures that the correct projected atomic potential is used for a given slice:

$$\psi\left(z+\Delta z\right)=\exp\left[\Delta z\frac{\lambda i}{4\pi}\nabla_{xy}^{2}+i\sigma\bar{V}\right]\psi+O\left(\Delta z^{2}\right) \tag{2.15}$$

Unfortunately, as equation 2.15 contains exponential operators, it cannot be easily evaluated. A Taylor series expansion of equation 2.15 would lead to a complicated and difficult-to-evaluate function, so equation 2.15 is simplified by casting the exponential term into a form more suitable for evaluation. Let,

$$A=\frac{i\lambda}{4\pi}\nabla_{xy}^{2} \tag{2.16}$$

$$B=\frac{i\sigma\bar{V}}{\Delta z} \tag{2.17}$$

and substituting equations 2.16 and 2.17 into equation 2.15 allows equation 2.15 to be rewritten as:

$$\psi\left(z+\Delta z\right)=\exp\left[A\Delta z+B\Delta z\right]\psi+O\left(\Delta z^{2}\right) \tag{2.18}$$

Desiring to find to what accuracy one may write,

$$\exp\left[A\Delta z+B\Delta z\right]=\exp\left[A\Delta z\right]\exp\left[B\Delta z\right] \tag{2.19}$$

a Taylor series is used to expand equation 2.18 to second order accuracy,

$$\exp\left[A\Delta z + B\Delta z\right] = 1 + \left(A + B\right)\Delta z + \frac{1}{2}\left(A^2 + B^2 + AB + BA\right)\Delta z^2 + O\left(\Delta z^3\right) \tag{2.20}$$

and a similar expansion is performed on $\exp\left[A\Delta z\right]\exp\left[B\Delta z\right]$:

$$\begin{aligned}\exp\left[A\Delta z\right]\exp\left[B\Delta z\right] &= \left[1 + A\Delta z + A^2\Delta z^2 + O\left(\Delta z^3\right)\right] \\ &\quad \cdot \left[1 + B\Delta z + B^2\Delta z^2 + O\left(\Delta z^3\right)\right] \\ &= 1 + \left(A + B\right)\Delta z + \frac{1}{2}\left(A^2 + B^2 + AB\right)\Delta z^2 \end{aligned} \tag{2.21}$$

To find the error in approximating $\exp\left[A\Delta z + B\Delta z\right]$ as $\exp\left[A\Delta z\right]\exp\left[B\Delta z\right]$, equation 2.21 is subtracted from equation 2.20 to give:

$$\begin{aligned}\exp\left[A\Delta z + B\Delta z\right] - \exp\left[A\Delta z\right]\exp\left[B\Delta z\right] &= \frac{1}{2}BA\Delta z^2 - \frac{1}{2}AB\Delta z^2 + O\left(\Delta z^3\right) \\ &= \frac{\Delta z^2}{2}\left[B, A\right] + O\left(\Delta z^3\right)\end{aligned} \tag{2.22}$$

Therefore, $\psi\left(z + \Delta z\right)$ can be approximated to first order accuracy in Δz as:

$$\psi\left(z + \Delta z\right) = \exp\left[\frac{i\lambda}{4\pi}\nabla^2_{xy}\Delta z\right]\exp\left[i\sigma\bar{V}\right]\psi + O\left(\Delta z^2\right) \tag{2.23}$$

The standard multislice method is computationally very efficient since equations of the form of 2.23 can be structured to use fast fourier transform (FFT) based algorithms. Let $t = \exp\left[i\sigma\bar{V}\right]$ be the transmission function for a given slice and substituting in equation 2.23:

$$\psi\left(z + \Delta z\right) = \exp\left[\frac{i\lambda}{4\pi}\nabla^2_{xy}\Delta z\right]\left(t\psi\right) + O\left(\Delta z^2\right) \tag{2.24}$$

Fourier transforming the resulting equation allows the evaluation of the exponential operators:

$$\begin{aligned}
FT_{xy}\left[\psi\left(z+\Delta z\right)\right] &= FT_{xy}\left[\exp\left(\frac{i\lambda\Delta z}{4\pi}\nabla^2_{xy}\right)(t\psi)\right] \\
&= \int\int \exp\left(\frac{i\lambda\Delta z}{4\pi}\nabla^2_{xy}\right)(t\psi)\exp\left(2\pi i\left[k_x x + k_y y\right]\right)dxdy \\
&= \int\int \exp\left(\frac{i\lambda\Delta z}{4\pi}\frac{\partial^2}{\partial x^2}\right)\exp\left(\frac{i\lambda\Delta z}{4\pi}\frac{\partial^2}{\partial y^2}\right)(t\psi) \\
&\quad \cdot \exp\left(2\pi i\left[k_x x + k_y y\right]\right)dxdy
\end{aligned} \tag{2.25}$$

Noting that the commutator $\left[\frac{\partial}{\partial x}, \frac{\partial}{\partial y}\right] = 0$, the exponential ∇^2_{xy} term can be separated without introducing further error. Hence equation 2.25 is uncoupled in x and y and may be written as:

$$FT_{xy}\left[\psi\left(z+\Delta z\right)\right] = FT_y\left[\exp\left(\frac{i\lambda\Delta z}{4\pi}\frac{\partial^2}{\partial y^2}\right)FT_x\left[\exp\left(\frac{i\lambda\Delta z}{4\pi}\frac{\partial^2}{\partial x^2}\right)(t\psi)\right]\right] \tag{2.26}$$

Expanding the exponential derivatives in 2.26,

$$\exp\left(\frac{i\lambda\Delta z}{4\pi}\frac{\partial^2}{\partial x^2}\right) = \sum_{n=0}^{\infty}\frac{1}{n!}\left(\frac{i\lambda\Delta z}{4\pi}\right)^n\left(\frac{\partial^2}{\partial x^2}\right)^n \tag{2.27}$$

and substituting the result into 2.26 leads to:

$$\begin{aligned}
FT_x\left[\exp\left(\frac{i\lambda\Delta z}{4\pi}\frac{\partial^2}{\partial x^2}\right)(t\psi)\right] &= \int\left[\sum_{n=0}^{\infty}\frac{1}{n!}\left(\frac{i\lambda\Delta z}{4\pi}\right)^n\left(\frac{\partial^2}{\partial x^2}\right)^n(t\psi)\right]\exp\left(-2\pi i\left[k_x x\right]\right)dx \\
&= \sum_{n=0}^{\infty}\frac{1}{n!}\left(\frac{i\lambda\Delta z}{4\pi}\right)^n\int\left[\left(\frac{\partial^2}{\partial x^2}\right)^n(t\psi)\right]\exp\left(-2\pi i\left[k_x x\right]\right)dx \\
&= \sum_{n=0}^{\infty}\frac{1}{n!}\left(\frac{i\lambda\Delta z}{4\pi}\right)^n\int\left[\left(\frac{\partial^2}{\partial x^2}\right)^n FT_x^{-1}\left[FT_x\left(t\psi\right)\right]\right] \\
&\quad\cdot\exp\left(-2\pi i\left[k_x x\right]\right)dx \\
&= \sum_{n=0}^{\infty}\frac{1}{n!}\left(\frac{i\lambda\Delta z}{4\pi}\right)^n\int\left[FT_x^{-1}\left[\left(\frac{\partial^2}{\partial x^2}\right)^n FT_x\left(t\psi\right)\right]\right] \\
&\quad\cdot\exp\left(-2\pi i\left[k_x x\right]\right)dx \\
&= \sum_{n=0}^{\infty}\frac{1}{n!}\left(\frac{i\lambda\Delta z}{4\pi}\right)^n\int\left[\int\left(\frac{\partial^2}{\partial x^2}\right)^n FT_x\left(t\psi\right)\right. \\
&\quad\left.\cdot\exp\left(2\pi i\left[k_x x\right]\right)dk_x\right]\exp\left(-2\pi i\left[k_x x\right]\right)dx \\
&= \sum_{n=0}^{\infty}\frac{1}{n!}\left(\frac{i\lambda\Delta z}{4\pi}\right)^n\int\left(4\pi^2 i^2 k_x^2\right)^n(t\psi)\exp\left(-2\pi i\left[k_x x\right]\right)dx \\
&= \sum_{n=0}^{\infty}\frac{1}{n!}\left(\frac{i\lambda\Delta z}{4\pi}\right)^n\left(4\pi^2 i^2 k_x^2\right)^n FT_x\left(t\psi\right) \\
&= \sum_{n=0}^{\infty}\frac{1}{n!}\left(-i\pi k_x^2\lambda\Delta z\right)^n FT_x\left(t\psi\right) \\
&= \exp\left(-i\pi k_x^2\lambda\Delta z\right)FT_x\left(t\psi\right) \qquad (2.28)
\end{aligned}$$

Subsequently, performing a Fourier transform in y reduces equation 2.26 to:

$$\begin{aligned}
FT_{xy}\left[\psi\left(z+\Delta z\right)\right] &= FT_y\left[\exp\left(\frac{i\lambda\Delta z}{4\pi}\frac{\partial^2}{\partial y^2}\right)FT_x\left[\exp\left(\frac{i\lambda\Delta z}{4\pi}\frac{\partial^2}{\partial x^2}\right)(t\psi)\right]\right] \\
&= FT_y\left[\exp\left(\frac{i\lambda\Delta z}{4\pi}\frac{\partial^2}{\partial y^2}\right)\exp\left[-i\pi\lambda\Delta z k_x^2\right]FT_x\left[t\psi\right]\right] \\
&= \exp\left[-i\pi\lambda\Delta z k_x^2\right]FT_y\left[\exp\left(\frac{i\lambda\Delta z}{4\pi}\frac{\partial^2}{\partial y^2}\right)FT_x\left[t\psi\right]\right] \\
&= \exp\left[-i\pi\lambda\Delta z\left(k_x^2+k_y^2\right)\right]FT_{xy}\left[t\psi\right] \\
&= P\left(k_x,k_y\right)FT_{xy}\left[t\psi\right] \qquad (2.29)
\end{aligned}$$

where the propagator function, $P\left(k_x, k_y\right)$, is given by:

$$P\left(k_x, k_y\right)=\exp\left[-i\pi\lambda\Delta z\left(k_x^2+k_y^2\right)\right] \tag{2.30}$$

By taking the inverse Fourier transform of equation 2.29, the solution to 2.24 may be written to first order accuracy in Δz as:

$$\psi\left(z+\Delta z\right)=FT_{xy}^{-1}\left[P\left(k_x, k_y\right)FT_{xy}\left(t\psi\right)\right]+O\left(\Delta z^2\right) \tag{2.31}$$

It is worth noting that there is another completely equivalent form of the multislice solution which results from factoring $\exp\left(A\Delta z+B\Delta z\right)$ as $\exp\left(B\Delta z\right)\exp\left(A\Delta z\right)$ rather than as $\exp\left(A\Delta z\right)\exp\left(B\Delta z\right)$. Following the same derivation presented above, the solution becomes:

$$\psi\left(z+\Delta z\right)=tFT_{xy}^{-1}\left[P\left(k_x, k_y\right)FT_{xy}\left(\psi\right)\right]+O\left(\Delta z^2\right) \tag{2.32}$$

Examining the expansion of $\exp\left(A\Delta z\right)\exp\left(B\Delta z\right)$ and $\exp\left(B\Delta z\right)\exp\left(A\Delta z\right)$ more closely, if can be shown that $\exp\left(A\Delta z+B\Delta z\right)$ may be factored as:

$$\begin{aligned}\exp\left(A\Delta z+B\Delta z\right)&=1+\Delta z\left(A+B\right)+\Delta z^2\left(A^2+AB+BA+B^2\right)+O\left(\Delta z^3\right)\\&=\frac{1}{2}\left[\exp\left(A\Delta z\right)\exp\left(B\Delta z\right)+\exp\left(B\Delta z\right)\exp\left(A\Delta z\right)\right]+O\left(\Delta z^3\right)\end{aligned} \tag{2.33}$$

Thus, if we average equations 2.31 and 2.32, the solution becomes, to one higher order of accuracy in Δz:

$$\begin{aligned}\psi\left(z+\Delta z\right)=&\frac{1}{2}FT_{xy}^{-1}\left[P\left(k_x, k_y\right)FT_{xy}\left(t\psi\right)\right]+\frac{1}{2}tFT_{xy}^{-1}\left[P\left(k_x, k_y\right)FT_{xy}\left(\psi\right)\right]\\&+O\left(\Delta z^3\right)\end{aligned} \tag{2.34}$$

In the following sections, the results and methodology developed in this section will be used to develop new multislice algorithms which attempt to include the contribution from the neglected second derivative term.

2.3 Second Derivative Multislice Derivation

In this section a version of the multislice solution that includes the second derivative term is derived. The reason for this was two fold; first to provide a more accurate solution which can act as a reference solution for more approximate methods, and secondly to test the approximation that $\left\| \frac{\partial^2 \psi}{\partial z^2} \right\| \ll \left\| \frac{4\pi i}{\lambda} \frac{\partial \psi}{\partial z} \right\|$ and that the second derivative term is therefore unimportant.

Although this method is shown to be unstable in section 3.3, the derivation is presented below for the sake of completeness and because it pertains to research performed during the summer of 2011. Hopefully the reader will be able to gain insight from this section and avoid similar problems of their own.

Following a similar derivation as given in section 2.2, rearrange equation 2.6 for $\frac{\partial \psi}{\partial z}$,

$$\frac{\partial \psi}{\partial z} = \frac{\lambda i}{4\pi} \left(\nabla_{xy}^2 \psi + \frac{\partial^2 \psi}{\partial z^2} \right) + i\sigma V \psi \tag{2.35}$$

and expand $\psi(z + \Delta z)$ in a Taylor series about z yielding:

$$\psi(z + \Delta z) = \left[1 + \Delta z \left(\frac{\lambda i}{4\pi} \left[\nabla_{xy}^2 + \frac{\partial^2}{\partial z^2} \right] + i\sigma V \right) \right] \psi + O\left(\Delta z^2\right) \tag{2.36}$$

As with equation 2.14, equation 2.36 can be cast into an exponential form as:

$$\psi(z + \Delta z) = \exp\left[\Delta z \left(\frac{\lambda i}{4\pi} \left[\nabla_{xy}^2 + \frac{\partial^2}{\partial z^2} \right] \right) + i\sigma \bar{V} \right] \psi + O\left(\Delta z^2\right) \tag{2.37}$$

Letting $t = \exp\left[i\bar{V} \right]$ as before, and performing the exponential expansion as in the previous section reduces equation 2.37 to:

$$\psi(z + \Delta z) = \exp\left[\frac{i\lambda}{4\pi} \nabla_{xy}^2 \Delta z \right] \exp\left[\frac{i\lambda}{4\pi} \frac{\partial^2}{\partial z^2} \Delta z \right] (t\psi) + O\left(\Delta z^2\right) \tag{2.38}$$

Finally, equation 2.38 can be evaluated through the use of Fourier transforms. Noting that the commutators $\left[\frac{\partial}{\partial x}, \frac{\partial}{\partial y} \right] = \left[\frac{\partial}{\partial y}, \frac{\partial}{\partial z} \right] = \left[\frac{\partial}{\partial z}, \frac{\partial}{\partial x} \right] = 0$, the Fourier transforms in x and y can be separated to yield:

$$\begin{aligned}
FT_{xy}\left[\psi\left(z+\Delta z\right)\right] &= \exp\left(\frac{i\lambda\Delta z}{4\pi}\frac{\partial^2}{\partial z^2}\right)P\left(k_x,k_y\right)FT_{xy}\left[t\psi\right] \\
&= \exp\left(\frac{i\lambda\Delta z}{4\pi}\frac{\partial^2}{\partial z^2}\right)P\left(k_x,k_y\right)FT_{xy}\left[t\psi\right] \\
&= \sum_{n=0}^{\infty}\frac{1}{n!}\left(\frac{i\lambda\Delta z}{4\pi}\right)^n\left(\frac{\partial^2}{\partial z^2}\right)^n P\left(k_x,k_y\right)FT_{xy}\left[t\psi\right] \\
&\approx \left(1+\frac{i\lambda\Delta z}{4\pi}\frac{\partial^2}{\partial z^2}\right)P\left(k_x,k_y\right)FT_{xy}\left[t\psi\right] \qquad (2.39)
\end{aligned}$$

By taking the inverse Fourier transform of equation 2.39, the solution to may be written to first order accuracy in Δz as:

$$\begin{aligned}
\psi\left(z+\Delta z\right) &= FT_{xy}^{-1}\left[\left(1+\frac{i\lambda\Delta z}{4\pi}\frac{\partial^2}{\partial z^2}\right)P\left(k_x,k_y\right)FT_{xy}\left[t\psi\right]\right]+O\left(\Delta z^2\right) \\
&= \left(1+\frac{i\lambda\Delta z}{4\pi}\frac{\partial^2}{\partial z^2}\right)FT_{xy}^{-1}\left[P\left(k_x,k_y\right)FT_{xy}\left[t\psi\right]\right]+O\left(\Delta z^2\right) \qquad (2.40)
\end{aligned}$$

In common with the standard multislice solution derived in section 2.2, the second derivative multislice solution has a number of equally valid alternate forms. Whereas there were two possible ways to rearrange the exponentials in the standard multislice solution, there are now six possible way to arrange the new solution:

$$\psi\left(z+\Delta z\right) = \left(1+\frac{i\lambda\Delta z}{4\pi}\frac{\partial^2}{\partial z^2}\right)FT_{xy}^{-1}\left[P\left(k_x,k_y\right)FT_{xy}\left[t\psi\right]\right]+O\left(\Delta z^2\right) \qquad (2.41)$$

$$\psi\left(z+\Delta z\right) = \left(1+\frac{i\lambda\Delta z}{4\pi}\frac{\partial^2}{\partial z^2}\right)tFT_{xy}^{-1}\left[P\left(k_x,k_y\right)FT_{xy}\left[\psi\right]\right]+O\left(\Delta z^2\right) \qquad (2.42)$$

$$\psi\left(z+\Delta z\right) = FT_{xy}^{-1}\left[\left(1+\frac{i\lambda\Delta z}{4\pi}\frac{\partial^2}{\partial z^2}\right)P\left(k_x,k_y\right)FT_{xy}\;t[\psi]\right]+O\left(\Delta z^2\right) \qquad (2.43)$$

$$\psi\left(z+\Delta z\right) = tFT_{xy}^{-1}\left[\left(1+\frac{i\lambda\Delta z}{4\pi}\frac{\partial^2}{\partial z^2}\right)P\left(k_x,k_y\right)FT_{xy}\left[\psi\right]\right]+O\left(\Delta z^2\right) \qquad (2.44)$$

$$\psi\left(z+\Delta z\right) = FT_{xy}^{-1}\left[P\left(k_x,k_y\right)FT_{xy}\left[\left(1+\frac{i\lambda\Delta z}{4\pi}\frac{\partial^2}{\partial z^2}\right)t\psi\right]\right]+O\left(\Delta z^2\right) \qquad (2.45)$$

$$\psi\left(z+\Delta z\right) = tFT_{xy}^{-1}\left[P\left(k_x,k_y\right)FT_{xy}\left[\left(1+\frac{i\lambda\Delta z}{4\pi}\frac{\partial^2}{\partial z^2}\right)\psi\right]\right]+O\left(\Delta z^2\right) \qquad (2.46)$$

If the second derivative terms are neglected, the above equations reduce to those obtained in section 2.2 for the standard multislice solutions.

2.4 Wave Solution Derivation

Due to the fact that the solution presented in section 2.3 was found to be unstable, an alternative method which preserved the second order derivative was derived. Owing to time constraints this method was not implemented in code, however the stability analysis presented in the next chapter suggests this method should be stable.

A third technique to solve equation 2.6 was developed using a Method of Lines (MOL) algorithm. Due to time constraints, this technique is not presented in detail, but the theory is provided as stimulus for future investigation.

In a MOL solution, the partial differential equation (PDE) being investigated is discretized in all but one dimension (the “time” dimension) into a system of coupled ordinary differential equations (ODEs). The coupling terms are evaluated before the start of the integration and assumed constant over the range of the integration (a single slice). This results in a system of decoupled differential equations which may be independently integrated over small time steps.

As related to the Schrödinger equation for fast electrons, the PDE 2.6 is subdivided into a two dimensional grid of ODEs with the potential and Laplacian terms assumed constant over a single slice (the average potential will be in the place of the point potential for increased accuracy). In this approximation, and using primed notation to highlight the discretization into a system of ODEs in z, equation 2.6 becomes:

$$\psi_{xy}^{''} + \frac{4\pi i}{\lambda}\psi_{xy}^{'} + \left(\nabla_{xy}^2 + \frac{2meV}{\hbar^2}\right)\psi_{xy} = 0 \tag{2.47}$$

Making the following variable substitutions and noting that equation 2.47 has the form of a second order ODE,

$$a = 1 \tag{2.48}$$

$$b = \frac{4\pi i}{\lambda} \tag{2.49}$$

$$c = c^{'} + c^{''} = \frac{2meV}{\hbar^2} + \nabla_{xy}^2 \tag{2.50}$$

allows the solution to equation 2.47 to be written as:

$$\psi_{xy}\left(z+\Delta z\right)=\exp\left(\left[\frac{-b}{2a}+\frac{\sqrt{b^2-4ac}}{2a}\right]\Delta z\right)d_{+xy}+\exp\left(\left[\frac{-b}{2a}-\frac{\sqrt{b^2-4ac}}{2a}\right]\Delta z\right)d_{-xy} \tag{2.51}$$

The eigen-solutions to 2.51 are therefore (note that $d_{\pm xy}$ are functions of x and y):

$$\begin{aligned}\psi_{\pm xy}\left(z+\Delta z\right)&=\exp\left(\left[\frac{-b}{2a}\pm\frac{\sqrt{b^2-4ac}}{2a}\right]\Delta z\right)d_{\pm xy}\\&=\exp\left(\left[\frac{-b}{2a}\pm\frac{b\sqrt{1-\frac{4ac}{b^2}}}{2a}\right]\Delta z\right)d_{\pm xy}\end{aligned} \tag{2.52}$$

Since $1-4ac/b^2\approx 1$, except perhaps very close to the core of an atom, the term under the radical can be approximated by a binomial expansion,

$$\begin{aligned}\sqrt{b^2-4ac}&=b\sqrt{1-\frac{4ac}{b^2}}\\&=b\sqrt{1-\frac{4a\left(c^{'}+c^{''}\right)}{b^2}}\\&\approx b-\frac{2a\left(c^{'}+c^{''}\right)}{b}\end{aligned} \tag{2.53}$$

and the eigenfunctions (equation 2.52) are given by:

$$\begin{aligned}\psi_{\pm xy}\left(z+\Delta z\right)&=\exp\left(\frac{-b}{2a}\Delta z\right)\exp\left(\frac{\pm b}{2a}\Delta z\right)\exp\left(\frac{\mp c^{'}}{b}\Delta z\right)\exp\left(\frac{\mp c^{''}}{b}\Delta z\right)d_{\pm xy}\\&=\exp\left(\frac{-2\pi i}{\lambda}\Delta z\right)\exp\left(\frac{\pm 2\pi i}{\lambda}\Delta z\right)\exp\left(\frac{\pm ime\lambda V}{2\pi\hbar^2}\Delta z\right)\\&\quad\cdot\exp\left(\frac{\pm i\lambda\Delta z}{4\pi}\nabla^2_{xy}\right)d_{\pm xy}\end{aligned} \tag{2.54}$$

The solution given by equation 2.54 is not particularly useful as the $\exp\left(\frac{\pm i\lambda\Delta z}{4\pi}\nabla^2_{xy}\right)$ term cannot be evaluated directly. However, noting that only the final term in equation 2.54 is dependant on x and y, and following the same procedure and notation outlined in section

2.2, equation 2.54 can be written as:

$$\begin{aligned}\psi_{\pm_{xy}}(z+\Delta z) &= \exp\left(\frac{-2\pi i}{\lambda}\Delta z\right)\exp\left(\frac{\pm 2\pi i}{\lambda}\Delta z\right)\exp\left(\frac{\pm ime\lambda V}{2\pi\hbar^2}\Delta z\right)\\ &\quad\cdot FT_{xy}^{-1}\left[FT_{xy}\left[\exp\left(\frac{\pm i\lambda\Delta z}{4\pi}\nabla_{xy}^2\right)d_{\pm_{xy}}\right]\right]\\ &= \exp\left(\frac{-2\pi i}{\lambda}\Delta z\right)\exp\left(\frac{\pm 2\pi i}{\lambda}\Delta z\right)\exp\left(\frac{\pm ime\lambda V}{2\pi\hbar^2}\Delta z\right)\\ &\quad\cdot FT_{xy}^{-1}\left[\exp\left(\mp i\pi\lambda\Delta z\left(k_x^2+k_y^2\right)\right)FT_{xy}\left[d_{\pm_{xy}}\right]\right]\end{aligned} \tag{2.55}$$

Therefore the two eigenfunctions are (if we replace $\exp\left(\frac{\pm ime\lambda V}{2\pi\hbar^2}\Delta z\right)$ with $\exp\left(i\sigma\bar{V}\right)$ as in section 2.2):

$$\psi_{+_{xy}}(z+\Delta z) = \exp\left(i\sigma\bar{V}\right)FT_{xy}^{-1}\left[\exp\left(-i\pi\lambda\Delta z\left(k_x^2+k_y^2\right)\right)FT_{xy}\left[d_{+_{xy}}\right]\right] \tag{2.56}$$

$$\begin{aligned}\psi_{-_{xy}}(z+\Delta z) &= \exp\left(\frac{-4\pi i}{\lambda}\Delta z\right)\exp\left(-i\sigma\bar{V}\right)FT_{xy}^{-1}\left[\exp\left(i\pi\lambda\Delta z\left(k_x^2+k_y^2\right)\right)\right.\\ &\quad\left.\cdot FT_{xy}\left[d_{-_{xy}}\right]\right]\end{aligned} \tag{2.57}$$

Interestingly, equation 2.56 is the solution to the standard multislice solution if $d_{+_{xy}} = \psi(z)$. One could then use initial conditions defining the value of the wave function, $\Omega(x,y)$, and its derivative, $\Theta(x,y)$, at (x,y,z),

$$\psi(x,y,z) = \Omega(x,y) \tag{2.58}$$

$$\frac{\partial\psi}{\partial z}(x,y,z) = \Theta(x,y) \tag{2.59}$$

to solve for $d_{+_{xy}}$ and $d_{-_{xy}}$ at the beginning of each slice.

2.5 Finite Difference Approximations

In addition to the multislice method, Kirkland proposes a second order finite difference solution for equation 2.1 [4]. Substituting the central, first order, finite difference approximations for $\frac{\partial\psi}{\partial z}$ and $\frac{\partial^2\psi}{\partial z^2}$,

$$\frac{\partial\psi\left(x,y,z\right)}{\partial z} = \frac{\psi\left(x,y,z+\Delta z\right)-\psi\left(x,y,z-\Delta z\right)}{2\Delta z} + O\left(\Delta z^2\right) \tag{2.60}$$

$$\frac{\partial^2\psi\left(x,y,z\right)}{\partial z^2} = \frac{\psi\left(x,y,z+\Delta z\right)-2\psi\left(x,y,z\right)+\psi\left(x,y,z-\Delta z\right)}{\Delta z^2} + O\left(\Delta z^2\right) \tag{2.61}$$

and rearranging for $\psi\left(x,y,z+\Delta z\right)$ yields a solution for equation 2.1 of significantly higher accuracy:

$$\psi\left(x,y,z+\Delta z\right) = \frac{1}{c_+}\left[2-\Delta z^2\left(\nabla^2_{xy}+\frac{4\pi\sigma}{\lambda}V\left(x,y,z\right)\right)\right]\psi\left(x,y,z\right)-\frac{c_-}{c_+}\psi\left(x,y,z\right)+O\left(\frac{\Delta z^4}{c_+}\right) \tag{2.62}$$

$$c_+ = 1+2\pi i\Delta z/\lambda \tag{2.63}$$

$$c_- = 1-2\pi i\Delta z/\lambda \tag{2.64}$$

$$\sigma = 2\pi me\lambda/h^2 \tag{2.65}$$

In equation 2.62, the $V\left(x,y,z\right)$ term represents an electrostatic potential at a single point. However, since the atomic potential function is sharply peaked near the center of each atom, this method of evaluation often either “skips” over the vast majority of an atomic potential or otherwise weighs the contribution of the atom incorrectly. This issue can be solved in part by reducing the slice thickness, but considering that atomic potentials obey roughly a $\frac{1}{r^2}$ dependance, reducing the slice thickness to the point were the atomic potential appears smooth is computationally inefficient. While running preliminary simulations, equation 2.62 was found to produce better results when $V\left(x,y,z\right)$ is replaced with the averaged potential

$\frac{1}{b-a}\int_a^b V(x,y,z_2)\,dz_2$. With this substitution, equation equation 2.62 becomes:

$$\begin{aligned}
\psi(x,y,z+\Delta z) &= \frac{1}{c_+}\left[2-\Delta z^2\left(\nabla^2_{xy}+\frac{4\pi\sigma}{\lambda}\frac{1}{b-a}\int_a^b V(x,y,z_2)\,dz_2\right)\right]\psi(x,y,z) \\
&- \frac{c_-}{c_+}\psi(x,y,z)+O\left(\frac{\Delta z^4}{c_+}\right) \qquad (2.66)
\end{aligned}$$

Due to stability issues encountered using equation 2.66 while evaluating CBED patterns, it was decided to write a MOL algorithm with a fourth order Runge-Kutta (RK4) integrator for the discretized ODEs. In the interest of expedient evaluation and ease of implementation, the algorithm used did not include error checking or adaptive step size control. As with the multislice method and finite difference solution, the PDE was evaluated on a rectangular region with periodic boundary conditions discretized in both the x and y directions (In order to use FFTs in the evaluation process it is necessary that the x and y discretizations be powers of 2).

Using an MOL evaluation procedure, equation 2.6 was reduced to a system of coupled ODE's which were then evaluated using RK4 integration for each z-step. At each point in the region, the PDE was discretized as:

$$\frac{d\psi_1}{dz} = \psi_2 \qquad (2.67)$$

$$\frac{d\psi_2}{dz} = -\nabla^2_{xy}\psi_1 - \frac{2meV}{\hbar^2}\psi_1 - \frac{4\pi i}{\lambda}\psi_2 \qquad (2.68)$$

where ψ_1 and ψ_2 are given by:

$$\psi_1(x,y,z) = \psi(x,y,z) \qquad (2.69)$$

$$\psi_2(x,y,z) = \frac{\partial\psi(x,y,z)}{\partial z} \qquad (2.70)$$

The evaluation of equations 2.67 and 2.68 is carried out simultaneously by the standard RK4 method which is reproduced for the reader's convenience below [8]. Let $y' = f(t,y)$

with $y(t_0) = y_0$. The RK4 solution is then:

$$k_1 = hf(t_n, y_n) \tag{2.71}$$

$$k_2 = hf\left(t_n + \frac{1}{2}h, y_n + \frac{1}{2}k_1\right) \tag{2.72}$$

$$k_3 = hf\left(t_n + \frac{1}{2}h, y_n + \frac{1}{2}k_2\right) \tag{2.73}$$

$$k_4 = hf(t_n + h, y_n + k_3) \tag{2.74}$$

$$t_{n+1} = t_n + h \tag{2.75}$$

$$y_{n+1} = y_n + \frac{1}{6}(k_1 + 2k_2 + 2k_3 + k_4) \tag{2.76}$$

It should be noted that as both of the finite difference methods described in this section are second order in z, the initial conditions must specify both the initial wave function and its z derivative. For the simulations presented in chapter 5, the initial derivative was determined by propagating the initial conditions backward several steps in z using the standard multislice method and then computed using finite differences.

Chapter 3

Stability Analysis

Before using one of the methods developed in Chapter 2, it is necessary to determine the conditions under which each can be used effectively. In general, it is desired to find the conditions under which each solution is stable. For the case of the multislice solution and wave solutions, it is shown that not only are the solutions unconditionally stable, but that probability is also conserved.

3.1 Background

This section uses a form of Fourier analysis similar to von Neumann stability analysis to determine the stability of the various multislice methods presented in Chapter 2. In a von Neumann stability analysis, the algorithm under investigation is applied to a set of initial conditions with a small error term (ϵ_n) resulting in a solution for the next time-step plus a new error term (ϵ_{n+1}) written in terms of algorithm variables (typically slice thickness, maximum spatial frequency and other such parameters). Subsequently, these error values are used to solve for the stability condition; the set of simulation conditions that cause the error term to remain constant or decay in time ($\left|\frac{\epsilon_{n+1}}{\epsilon_n}\right| \leq 1$).

In many cases, a Von Neumann analysis would be sufficient to demonstrate the conditions for stability. Although undeniably useful, finding the bandwidth limiting conditions which prevent a single spatial frequency from experiencing exponential growth is not the primary interest. Instead, the interest is in determining whether or not the norm of a solution is preserved from slice to slice. There is no problem if a particular spatial frequency grows in magnitude so long as that growth comes at the expense of other spatial frequencies. In physical terms, the wave function must remain normalized from slice to slice.

3.2 Multislice

The multislice solution has several advantages over other numerical methods used to solve PDEs. The most obvious of these is the speed by which the method can be evaluated through the use of FFTs and multicore processing. A more subtle advantage, which is demonstrated presently, is that the standard multislice method is unconditionally stable.

The magnitude of ψ is given by $\int\int \psi\psi^* dxdy$ and the magnitude of any function multiplied by a purely imaginary exponential is unchanged:

$$\begin{aligned}
\left\|\psi \exp\left(ia\left(x,y\right)\right)\right\|^2 &= \int\int \psi \exp\left(ia\left(x,y\right)\right)\psi^* \exp\left(-ia\left(x,y\right)\right)dxdy \\
&= \int\int \psi\psi^* \exp\left(ia\left(x,y\right) - ia\left(x,y\right)\right)dxdy \\
&= \int\int \psi\psi^* dxdy \\
&= \left\|\psi\right\|^2 \qquad (3.1)
\end{aligned}$$

In the case of the multislice solution, the transmission function, $t\left(x,y\right)$, is a purely imaginary function so that $\left\|\psi t\right\|^2 = \left\|\psi\right\|^2$. In order to save considerable mathematical difficulty in the following analysis, define $\psi_t = \psi t$.

It is known that the magnitudes of ψ_t, ψt and ψ are equal. Therefore, if ψ_t is used in place of ψt in equation 2.31, it is expected that the magnitude of $\psi\left(z + \Delta z\right)$ will be equal to that of ψ. In order to show this, ψ_t will be decomposed into an infinite Fourier series, the analysis performed for a single-frequency mode and subsequently the results generalized to the entire function.

Let ψ_t, ψt and ψ obey periodic boundary conditions with x and y defined on $[-a, a]$ and $[-b, b]$, respectively. Then ψ_t may be represented as a Fourier series:

$$\psi_t = \sum_m \sum_n a_{mn} \exp\left(2\pi i\left(k_{mx}x + k_{ny}y\right)\right) \qquad (3.2)$$

Since ψ is defined on $x \subset [-a, a]$ and $y \subset [-b, b]$, the only permitted values of k_{mx} and k_{ny} are $k_{mx} = \frac{m}{2a}$ and $k_{ny} = \frac{n}{2b}$:

$$\psi_t = \sum_m \sum_n a_{nm} \exp\left(\frac{im\pi x}{a}\right) \exp\left(\frac{in\pi y}{b}\right) \tag{3.3}$$

Using a discretized version of equation 2.31, a single frequency component is transformed as:

$$\begin{aligned}
\psi_{nm}(z + \Delta z) &= FT_{xy}^{-1}\left[\exp\left(-i\pi\lambda\Delta z\left(\frac{m'^2}{4a^2} + \frac{n'^2}{4b^2}\right)\right) FT_{xy}\left[a_{nm}\exp\left(\frac{im\pi x}{a} + \frac{in\pi y}{b}\right)\right]\right] \\
&= FT_{xy}^{-1}\left[\exp\left(-i\pi\lambda\Delta z\left(\frac{m'^2}{4a^2} + \frac{n'^2}{4b^2}\right)\right)\frac{1}{4ab}\int_{-a}^{a}\int_{-b}^{b} a_{nm}\right. \\
&\quad \left. \cdot \exp\left(\frac{im\pi x}{a} + \frac{in\pi y}{b}\right) \exp\left(\frac{-im'\pi x}{a} + \frac{-in'\pi y}{b}\right) dxdy\right] \\
&= FT_{xy}^{-1}\left[\exp\left(-i\pi\lambda\Delta z\left(\frac{m'^2}{4a^2} + \frac{n'^2}{4b^2}\right)\right) a_{nm}\delta_{mm'}\delta_{nn'}\right] \\
&= \sum_{m'}\sum_{n'} \exp\left(-i\pi\lambda\Delta z\left(\frac{m'^2}{4a^2} + \frac{n'^2}{4b^2}\right)\right) a_{nm}\delta_{mm'}\delta_{nn'} \exp\left(\frac{im'\pi x}{a} + \frac{in'\pi y}{b}\right) \\
&= a_{nm}\exp\left(-i\pi\lambda\Delta z\left(\frac{m^2}{4a^2} + \frac{n^2}{4b^2}\right)\right)\exp\left(\frac{im\pi x}{a} + \frac{in\pi y}{b}\right)
\end{aligned} \tag{3.4}$$

As shown in equation 3.1, the magnitude of each frequency component of ψ_t is preserved by the standard multislice algorithm. This is not to say that the magnitude of frequency components does not vary between ψ and $\psi(z + \Delta z)$, but that the magnitude of the frequency components of ψ_t and $\psi(z + \Delta z)$ is unchanged. Summing all of the frequency terms together, the solution to $\psi(z + \Delta z)$ is represented by:

$$\psi(z + \Delta z) = \sum_m \sum_n a_{nm} \exp\left(-i\pi\lambda\Delta z\left(\frac{m^2}{4a^2} + \frac{n^2}{4b^2}\right)\right) \exp\left(\frac{im\pi x}{a} + \frac{in\pi y}{b}\right) \tag{3.5}$$

To find the magnitude of $\psi\left(z+\Delta z\right)$, multiply by its complex conjugate and integrate over x and y:

$$\begin{aligned}\left\|\psi\left(z+\Delta z\right)\right\| &= \int_{-a}^{a}\int_{-b}^{b}\psi\left(z+\Delta z\right)\psi\left(z+\Delta z\right)^{*}dxdy\\ &= \int_{-a}^{a}\int_{-b}^{b}\left[\sum_{m,n}a_{nm}\exp\left(-i\pi\lambda\Delta z\left(\frac{m^2}{4a^2}+\frac{n^2}{4b^2}\right)\right)\exp\left(\frac{im\pi x}{a}+\frac{in\pi y}{b}\right)\right]\\ &\quad\cdot\left[\sum_{m,n}a_{mn}^{*}a_{nm}\exp\left(i\pi\lambda\Delta z\left(\frac{m^2}{4a^2}+\frac{n^2}{4b^2}\right)\right)\exp\left(\frac{-im\pi x}{a}+\frac{-in\pi y}{b}\right)\right]dxdy\end{aligned} \tag{3.6}$$

Due to the orthogonality of the basis functions, the cross terms cancel and equation 3.6 can be rewritten as:

$$\begin{aligned}\left\|\psi\left(z+\Delta z\right)\right\| &= \int_{-a}^{a}\int_{-b}^{b}\sum_{m}\sum_{n}a_{mn}a_{mn}^{*}\exp\left(-i\pi\lambda\Delta z\left(\frac{m^2}{4a^2}+\frac{n^2}{4b^2}\right)\right)\\ &\quad\cdot\exp\left(\frac{im\pi x}{a}+\frac{in\pi y}{b}\right)\exp\left(i\pi\lambda\Delta z\left(\frac{m^2}{4a^2}+\frac{n^2}{4b^2}\right)\right)\\ &\quad\cdot\exp\left(\frac{-im\pi x}{a}+\frac{-in\pi y}{b}\right)dxdy \qquad (3.7)\\ &= \int_{-a}^{a}\int_{-b}^{b}\sum_{m}\sum_{n}a_{mn}a_{mn}^{*}dxdy \qquad (3.8)\end{aligned}$$

which is exactly the same magnitude as ψ_t, ψt and ψ. Therefore, the multislice algorithm preserves the norm of the wave function to within numerical accuracy.

3.3 Second Derivative Multislice

Let: ψ obey periodic boundary conditions in x and y and and be defined on $x \subset [-a, a]$ and $y \subset [-b, b]$. Consider the case where the wave function does not necessarily obey periodic boundary conditions in z. A single frequency component of ψ_t can therefore be written as:

$$\psi_t = \sum_m \sum_n a_{nm} \exp\left(\frac{im\pi x}{a}\right) \exp\left(\frac{in\pi y}{b}\right) \exp\left(2\pi i k_z z\right) \tag{3.9}$$

Substituting equation 3.9 for $t\psi$ in equation 2.41 and simplifying as in section 3.2 gives:

$$\begin{aligned}
\psi\left(z + \Delta z\right) &= \left(1 + \frac{i\lambda\Delta z}{4\pi}\frac{\partial^2}{\partial z^2}\right) \exp\left(-i\pi\lambda\Delta z\left(\frac{m^2}{4a^2} + \frac{n^2}{4b^2}\right)\right) \\
&\quad \cdot a_{nm} \exp\left(\frac{im\pi x}{a} + \frac{in\pi y}{b} + 2\pi i k_z z\right) \\
&= \exp\left(-i\pi\lambda\Delta z\left(\frac{m^2}{4a^2} + \frac{n^2}{4b^2}\right)\right) a_{nm} \exp\left(\frac{im\pi x}{a} + \frac{in\pi y}{b} + 2\pi i k_z z\right) \\
&\quad \cdot \left(1 - i\lambda\Delta z\pi k_z^2\right)
\end{aligned} \tag{3.10}$$

Taking the magnitude of $\psi\left(z + \Delta z\right)$, $\|\psi\left(z + \Delta z\right)\| = \left(1 + \lambda^2\Delta z^2\pi^2 k_z^4\right) > 1$ for all possible choices of Δz. Therefore, the magnitude of any frequency component will grow without bound as the solution is advanced through the sample, resulting in massive instability. This is exactly the behaviour observed in simulations using this method.

Originally, when this method was first tested, the solutions were relatively stable and agreed very well with the standard multislice solution. It was discovered, however that there was an error in the code implementing the algorithm which acted to minimize the contributions of the second derivative term. Once this error was corrected, it became obvious that implementation of algorithms based on equation 2.41 were extremely unstable. It should be noted that the stability of equations 2.42 through 2.46 have not been investigated to date, but are expected to be likewise unstable.

3.4 Wave Solution

Examining equation 2.56, it is observed that the first eigenfunction of the wave solution has exactly the same form as equation 2.31 and should therefore be unconditionally stable. The only differences between the first and second eigenfunctions of the wave solution are the addition of an imaginary exponential prefactor and oppositely signed exponentials. For this reason, the analysis presented in 3.2 will hold for the second eigenfunction of the wave solution and the total wave solution should therefore be unconditionally stable.

3.5 Finite Difference Approximations

In [4], Kirkland uses a form of von Neumann stability analysis to determine the approximate conditions for stability required by the finite difference method discussed in section 2.5. It is shown that the maximum spatial frequency which permits stable free-space propagation is given by:

$$k_e^2 < \frac{1}{4\pi^2 z^2}\left[\sqrt{1 + 4\pi^2 \Delta z^2/\lambda^2} - 2\right] \tag{3.11}$$

However, due to time constraints, the finite difference methods were not thoroughly investigated.

The conditions for stability of the RK4 method were not investigated. As a result, the precise conditions for stability for the RK4 method are unknown. For the RK4 simulations presented in Chapter 5, the method was experimentally found to be stable when the slice thickness was decreased below 0.005 Å.

Chapter 4

Atomic Potentials

In this section the relationship between atomic scattering factors and atomic potentials is explored. Two methods of calculating the atomic potentials are introduced and the parameterization of the potentials and atomic scattering factors are compared.

4.1 The Born Approximation

The wave function resulting from a scattering event between an electron and a potential $V\left(\mathbf{r}'\right)$ may be obtained as an integral equation in $\psi\left(\mathbf{r}\right)$[6],

$$\psi\left(\mathbf{r}\right) = \phi_{inc}\left(\mathbf{r}\right) - \frac{\mu}{2\pi\hbar^2}\int_{-\infty}^{\infty}\frac{\exp\left(ik\left|\mathbf{r}-\mathbf{r}'\right|\right)}{\left|\mathbf{r}-\mathbf{r}'\right|}V\left(\mathbf{r}'\right)\psi\left(\mathbf{r}'\right)d^3r' \tag{4.1}$$

where $\phi_{inc}\left(\mathbf{r}\right)$ is the incident wave function and μ is the vacuum permeability. In the first approximation, $\psi\left(\mathbf{r}'\right)$ is substituted for $\phi_{inc}\left(\mathbf{r}\right)$ in the integrand. Making the far-field approximation, $r \gg r'$, results in the first Born approximation [6]:

$$\psi\left(\mathbf{r}\right) = \phi_{inc}\left(\mathbf{r}\right) - \frac{\mu}{2\pi\hbar^2}\int_{-\infty}^{\infty}\frac{\exp\left(-i\mathbf{k}\cdot\mathbf{r}'\right)}{\mathbf{r}}V\left(\mathbf{r}'\right)\phi_{inc}\left(\mathbf{r}'\right)d^3r' \tag{4.2}$$

Letting the incident wave function be given by a plane wave and setting $\mathbf{q} = \mathbf{k_0} - \mathbf{k}$, equation 4.2 reduces to:

$$\begin{aligned} \psi(\mathbf{r}) &= \exp\left(i\mathbf{k_0}\cdot\mathbf{r}'\right) - \frac{\mu}{2\pi\hbar^2\mathbf{r}}\int_{-\infty}^{\infty}\exp\left(i\left(\mathbf{k_0}-\mathbf{k}\right)\cdot\mathbf{r}'\right)V\left(\mathbf{r}'\right)d^3r' \\ &= \exp\left(i\mathbf{k_0}\cdot\mathbf{r}'\right) - \frac{\mu}{2\pi\hbar^2\mathbf{r}}\int_{-\infty}^{\infty}\exp\left(i\mathbf{q}\cdot\mathbf{r}'\right)V\left(\mathbf{r}'\right)d^3r' \end{aligned} \tag{4.3}$$

This may be simplified this further, by introducing the quantity $f(\theta,\phi)$, the electron scattering factor:

$$f(\theta,\phi) = \frac{\mu}{2\pi\hbar^2\mathbf{r}}\int_{-\infty}^{\infty}\exp\left(i\mathbf{q}\cdot\mathbf{r}'\right)V\left(\mathbf{r}'\right)d^3r \tag{4.4}$$

$$\psi(\mathbf{r}) = \exp\left(i\mathbf{k_0}\cdot\mathbf{r}'\right) - \frac{f(\theta,\phi)}{\mathbf{r}} \tag{4.5}$$

In the first Born approximation, therefore, the electron scattering factors are the three dimensional Fourier transform of the atomic potentials. Hence, to a first approximation, the atomic potential at a displacement $\mathbf{r}$ from an atomic nuclei may be calculated as (in the notation of Kirkland) [4]:

$$V(\mathbf{r}) = 2\pi e a_0\int_{-\infty}^{\infty}f_e(\mathbf{q})\exp(-2\pi i\mathbf{q}\cdot\mathbf{r})d^3q \tag{4.6}$$

$$f_e(\mathbf{q}) = \frac{1}{2\pi e a_0}\int_{-\infty}^{\infty}V(\mathbf{r})\exp(2\pi i\mathbf{q}\cdot\mathbf{r})d^3r \tag{4.7}$$

where $f_e(\mathbf{q})$ are the electron scattering factors, and $q = \sin(\alpha)/\lambda$ is the magnitude of the difference between the incident and scattered electron wavevectors [4] (in the formula above, α is the scattering semi-angle). Conversely, in the notation of Doyle and Turner [7], the scattering factors are parameterized according to $s = \sin(\alpha/2)/\lambda$, where $q \approx 2s$.

In the evaluation of the multislice method, the primary interest is in calculating the projected atomic potential between two slices for use in evaluating the transmission function:

$$t = \exp\left(i\int_{z}^{z+\Delta z}V(\mathbf{r})\,dz\right) \tag{4.8}$$

The integral in equation 4.8 may then be represented as:

$$\int_{z}^{z+\Delta z} V\left(\mathbf{r}\right) dz = 2\pi e a_0 \int_{z}^{z+\Delta z} \int_{-\infty}^{\infty} f_e\left(\mathbf{q}\right) \exp\left(-2\pi i \mathbf{q}\cdot\mathbf{r}\right) d^3q \; dz \tag{4.9}$$

In order to evaluate equation 4.9 efficiently, the electron scattering factors, $f_e\left(\mathbf{q}\right)$, must be parameterized such that the integral may be evaluated analytically.

4.2 Parameterization of Electron Scattering Factors

The electron scattering factors used in Kirkland [4] were fit using a combination of three Gaussian distributions and three Lorentzian distributions so as to give the correct form for the scattering factors at both low and high scattering angles. The parameterization used by Kirkland for the electron scattering factors takes the form[4],

$$f_e\left(q\right) = \sum_{i=1}^{3} \frac{a_i}{q^2 + b_i} + \sum_{i=1}^{3} c_i \exp\left(-d_i q^2\right) \tag{4.10}$$

where the constants a_i, b_i, c_i and d_i are fitting parameters. Using equations 4.6 and 4.10 the atomic potential a distance r from a given atomic nuclei is given by:

$$V\left(x, y, z\right) = 2\pi^2 a_0 e \sum_{i=1}^{3} \frac{a_i}{r} \exp\left(-2\pi r \sqrt{b_i}\right) + 2\pi^{5/2} a_0 e \sum_{i=1}^{3} c_i d_i^{-3/2} \exp\left(-\pi^2 r^2 / d_i\right) \tag{4.11}$$

Upon substituting equation 4.11 in equation 4.9, it is found that the projected atomic potential may be solved analytically only when the integral is over all z:

$$\int_{-\infty}^{\infty} V\left(\mathbf{r}\right) dz = 4\pi^2 a_0 e \sum_{i=1}^{3} a_i K_0\left(2\pi r \sqrt{bi}\right) + 2\pi^2 a_0 e \sum_{i=1}^{3} \frac{c_i}{d_i} \exp\left(-\pi^2 r^2 / d_i\right) \tag{4.12}$$

Although this enables equation 4.9 to be fit as a series of splines in $\rho = \sqrt{x^2 + y^2}$ and evaluated with great computational efficiency [4], there is a potential issue with Kirkland's formulation of the multislice solution as illustrated in Figure 4.1.

In order to be as accurate as possible it is desirable to integrate the atomic potential between z and $z + \Delta z$ such that there is a proper accounting of the contribution from all nearby atoms in the lattice (for the purpose of the simulation, any atom within 3 Å of the top or bottom of the slice was considered a contributor). Using the Kirkland formulation of the projected atomic potential, slices which contain no atoms are treated as propagating the electron through free space; the projected atomic potential calculation effectively ignores the contribution to the projected atomic potential from atoms outside the slice interval.

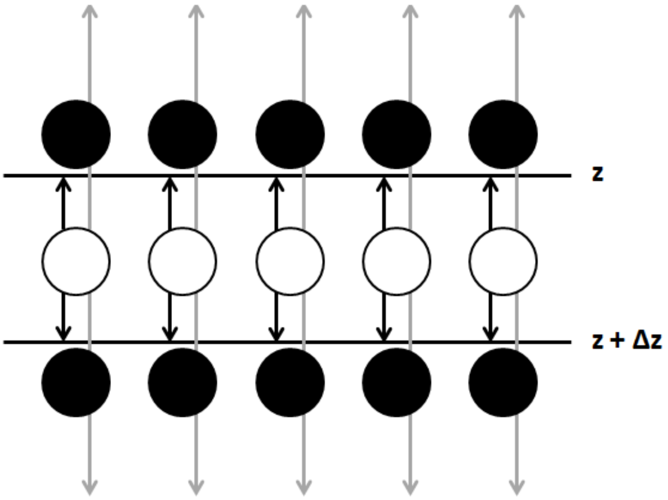

Figure 4.1: In Kirkland's formulation of the multislice method, only atoms between z and $z+\Delta z$ (shown in white) contribute to the projected atomic potential and their contribution is integrated from $-\infty$ to ∞. Ideally, neighbouring atoms (shown in black) would also contribute to the projected atomic potential and the contribution would be bounded by z and $z+\Delta z$.

According to Kirkland [4], this problem can be remedied in part by maintaining the slice thickness greater than one angstrom so that atoms are not "lost" in between the slices [4]. However, noting from equation 2.31 that the standard form of the multislice solution is only accurate to first order in Δz (depending on the order in which the transmissions and propagations are applied, the multislice solution may be actually interpreted as second order accurate in Δz [4, 3]). As such, when using the Kirkland formulation of the potential, one encounters the problem that if the slice thickness is too large, the multislice method may become inaccurate while if the slice thickness is too small, the transmission layer calculation may become inaccurate.

If the electron scattering factors are parameterized as Gaussians however, equation 4.9 can be solved analytically for any upper and lower bounds. This form of the projected atomic potential will be referred to as the bounded potential.

$$\int_{z}^{z+\Delta z} V(\mathbf{r})\, dz = \pi^2 a_0 e \sum_{i=1}^{n} \frac{c_i}{d_i} \exp\left(\frac{-\pi^2\left[x^2+y^2\right]}{d_i}\right)\left[\operatorname{erf}\left(\frac{\pi\left[z+\Delta z\right]}{\sqrt{d_i}}\right)+\operatorname{erf}\left(\frac{\pi z}{\sqrt{d_i}}\right)\right] \tag{4.13}$$

The Gaussian distributions used in the new simulations are those developed by Peng et al. [5]. Although the Gaussian distributions fail to completely account for the singular nature of the atomic potential near the atom, both the parameterizations developed by Kirkland and Peng were fit from $q = 0\mathring{A}$ to $q = 12$ Å [4, 5] ($s = 0$ Å to $s = 6$ Å in the notation of Doyle and Turner [4, 5, 7]). Thus, if angles of observation are restricted, results should remain consistent. For acceleration potentials of 100 KeV and 300 KeV, this condition becomes $\theta \leqslant 444$ mrad and $\theta \leqslant 236$ mrad, respectively.

4.3 Comparison of Electron Scattering Factors

The Peng (Gaussian parameterization) and Kirkland (Gaussian and Lorentzian parameterization) electron scattering factors for gold and silicon are plotted in Figures 4.2 and 4.3, respectively, for $q = 0$ Å^{-1} to $q = 12$ Å^{-1}. For both elements, the parameterizations are nearly identical out to 6 Å^{-1}, but begin to show some deviation from one another at higher angles.

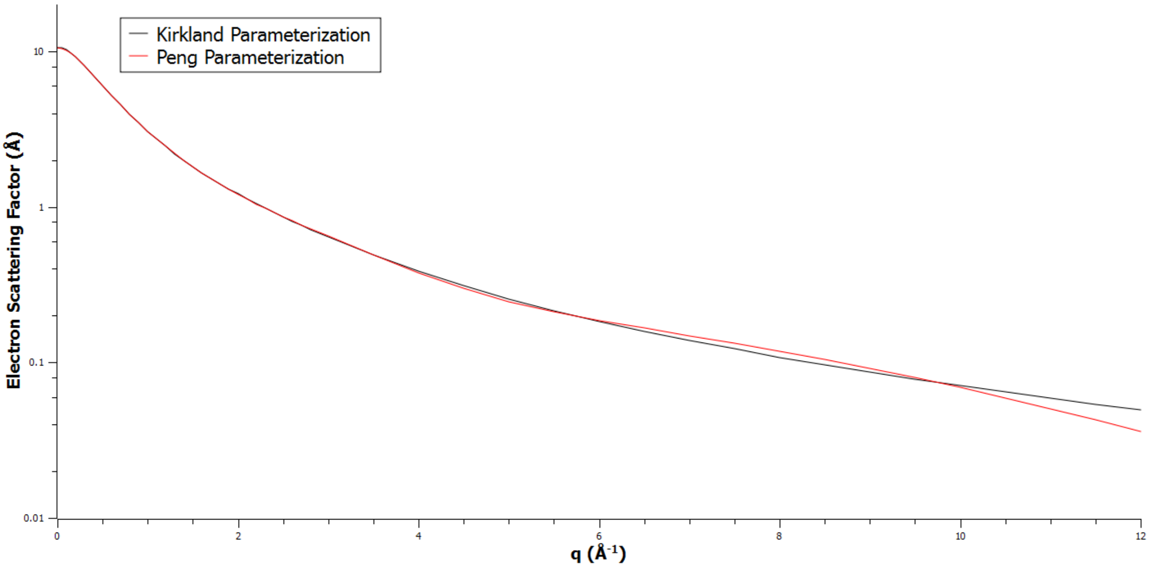

Figure 4.2: Kirkland and Peng electron scattering factors for gold plotted against the magnitude of the scattering vector. Note that the y axis has been log scaled.

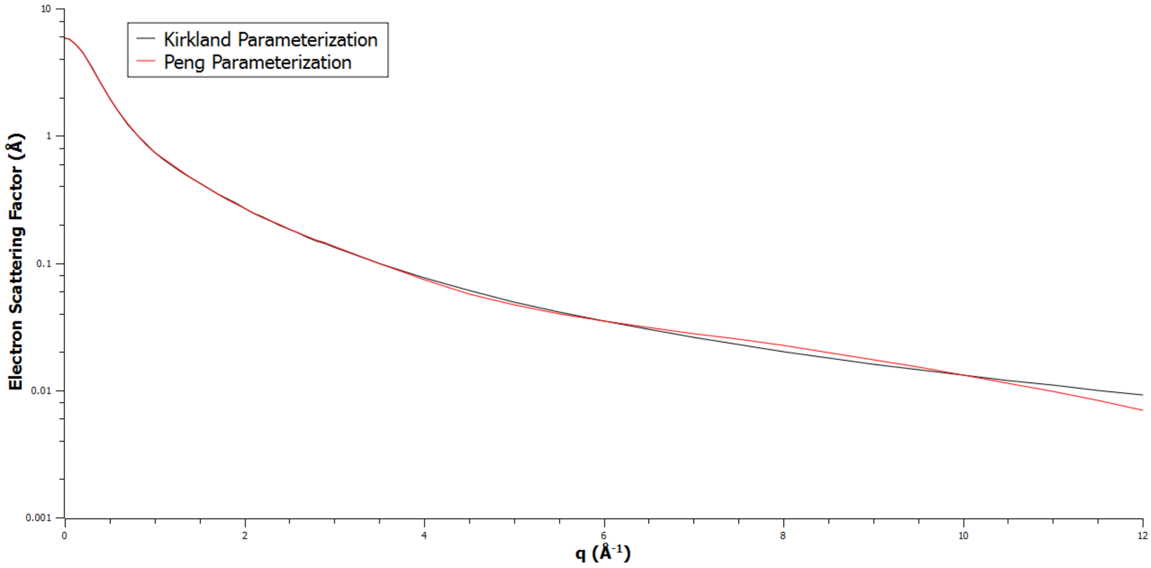

Figure 4.3: Kirkland and Peng electron scattering factors for silicon plotted against the magnitude of the scattering vector.

4.4 Comparison of Atomic Potentials

The Peng and Kirkland atomic potentials for gold and silicon are plotted in Figures 4.4 and 4.5 respectively, for $r = 0$ Å to $r = 0.8$ Å. For both elements, the parameterizations are nearly identical above 0.1 Å, but show substantial variation at small radii. This seemingly large variation is relatively unimportant, however, as any electrons which approach substantially close to the atoms to experience the potential difference will be scattered to extremely high angles.

The electron scattering factors are related to the atomic potentials through equations 4.6 and 4.7 which are essentially Fourier transforms. As the Peng electron scattering factors are parameterized by Gaussians and the Fourier transform of a Gaussian is likewise a Gaussian, the Peng parameterizations, unlike the Kirkland parameterizations, shown in Figures 4.4 and 4.5 are not singular at $r = 0$.

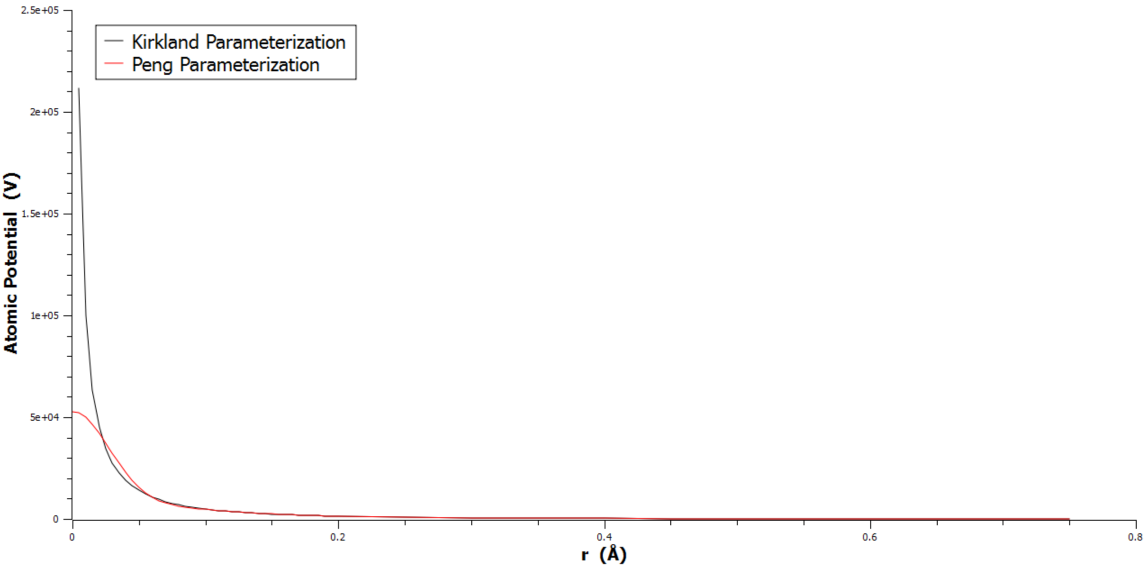

Figure 4.4: Kirkland (Gaussian and Lorentzian) and Peng (Gaussian) parameterizations of atomic potentials for gold plotted as a function of distance from the center of the atom

In the simulations, the electron approach distance is limited to about 0.01 Å for a 512 x 512 pixel simulation of a 20 x 20 Å sample. This limitation of the approach distance is justified as the electron scattering factors were parameterized up to $q = 12$ Å^{-1}. Hence,

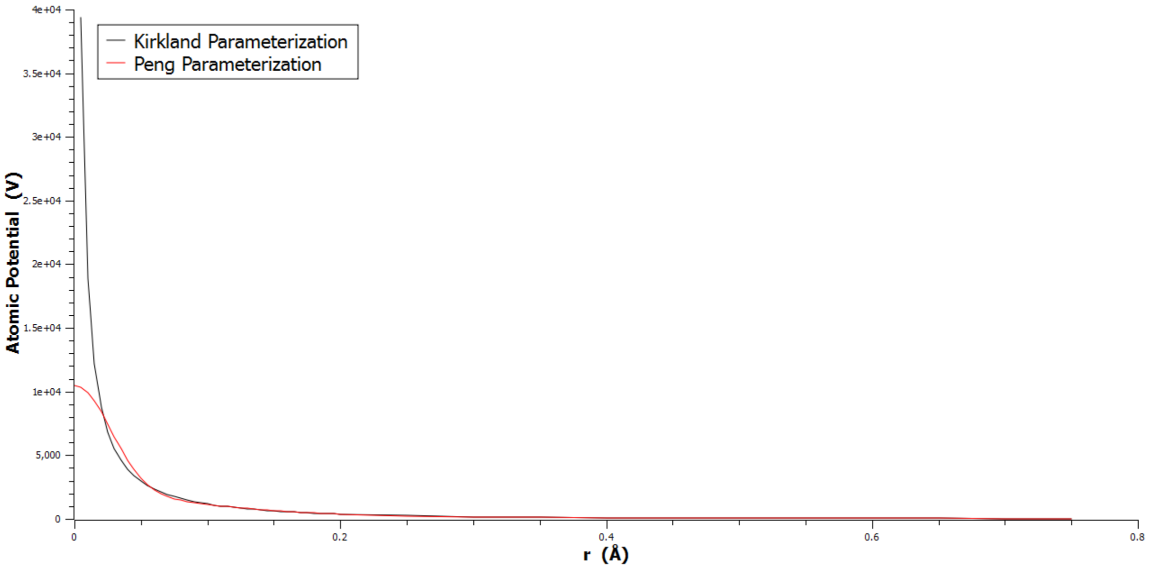

Figure 4.5: Kirkland (Gaussian and Lorentzian) and Peng (Gaussian) parameterizations of atomic potentials for silicon plotted as a function of distance from the center of the atom

any component of the electron wave function which approaches close enough to encounter a divergent potential will be scattered out to angles greater than those recorded.

Chapter 5

Comparison of Methods

This chapter presents a series of results comparing the potential integration schemes introduced in Chapter 4, a brief comparison of the standard multislice and RK4 methods, and some preliminary data on the effects of super cell size on CBED patterns. Due to time constraints, the utility of the wave solutions and finite difference schemes are not investigated.

5.1 Conditions and Methodology

Unless otherwise noted, the results presented in this chapter were calculated for [111] silicon using CM30 conditions, the input file for which may be found in Appendix A. The unit cell used was a 7.6792 Å x 13.3007 Å x 9.4050 Å rectangular basis of 48 silicon atoms tiled three times in the x direction, twice in the y direction and fifty four times in the z direction giving super cell x and y dimensions of 23.0376 Å and 26.6014 Å, respectively. The spherical aberration coefficient was set to 2.0 mm and the objective aperture was set to 3.1 mrad. For 300 KeV simulations, the average defocus value was set to 471 Å, while for 100 KeV simulations the average defocus value was set to 645 Å. The CBED probe itself was placed at the upper left hand corner of the cell at $x = 0$, $y = 0$.

The results are given for the first slice occurring after the 500 Å depth in the sample and are averaged over sixteen trials to account for thermal vibration effects (simulated by displacing the atoms in the lattice according to gaussian distributions). Hence, results for simulations run with different Δz will not correspond to exactly the same depth in the sample. In addition, the simulations run with bounded potentials were initiated approximately 3 Å above the top surface of the sample, while those run with unbounded potentials were initiated at the surface of the sample. Had the bounded potential calculations been initiated at the surface of the sample, half of the projected atomic potential of the first layer of atoms would have been neglected. Unless otherwise noted, the simulations were run with thermal vibrations effects included at a temperature of 300 K.

According to Kirkland, running simulations with slice thicknesses that differ substantially from an integer fraction of the unit cell depth can result in the appearance of artificial Laue zones. To eliminate the possibility of this occurrence, all simulations are run with slice thicknesses equal to fractions of the unit cell depth.

Figure 5.1 gives an example of the radially integrated CBED intensity shown beside the corresponding log scaled CBED pattern. The radially integrated intensity is typically measured outwards in mrads and this integration is performed in such a way that if the CBED pattern is stretched due to uneven super cell dimensions, the angular dependence of the radially integrated intensity plot is unaffected.

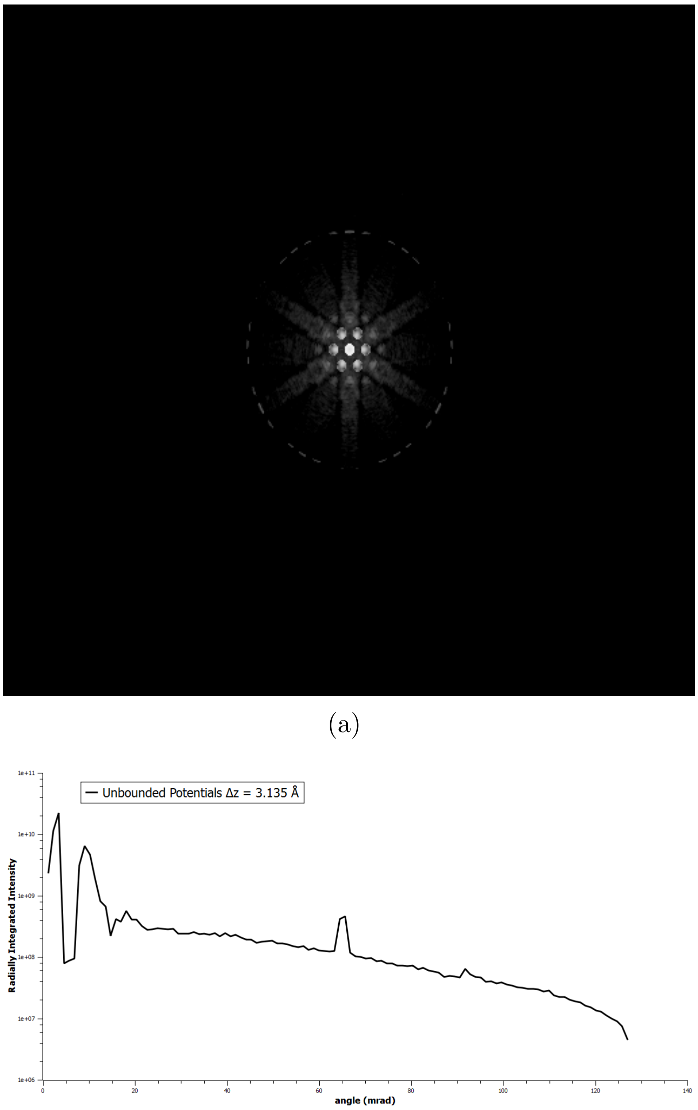

(a)

(b)

Figure 5.1: a) CBED pattern and b) corresponding graph of the radially integrated intensities for 50 nm of [111] silicon at 300 KeV using CM30 simulation conditions. The location of the zeroth order Laue zone (ZOLZ), first order Laue zone (FOLZ) and second order Laue zone (SOLZ) can be readily determined. Due to the uneven super cell dimensions, the CBED pattern a) has been stretched.

5.2 Thermal Variation

In order to accurately quantify the differences between the potential calculation methods presented in Chapter 4, it is crucial to know the typical variance within a given method. To quantify the variance within a single method, four identical simulations of [111] silicon were run at $\Delta z = 3.135$ Å for the case of unbounded potentials. The radially integrated intensities of the simulations are shown below in Figure 5.2.

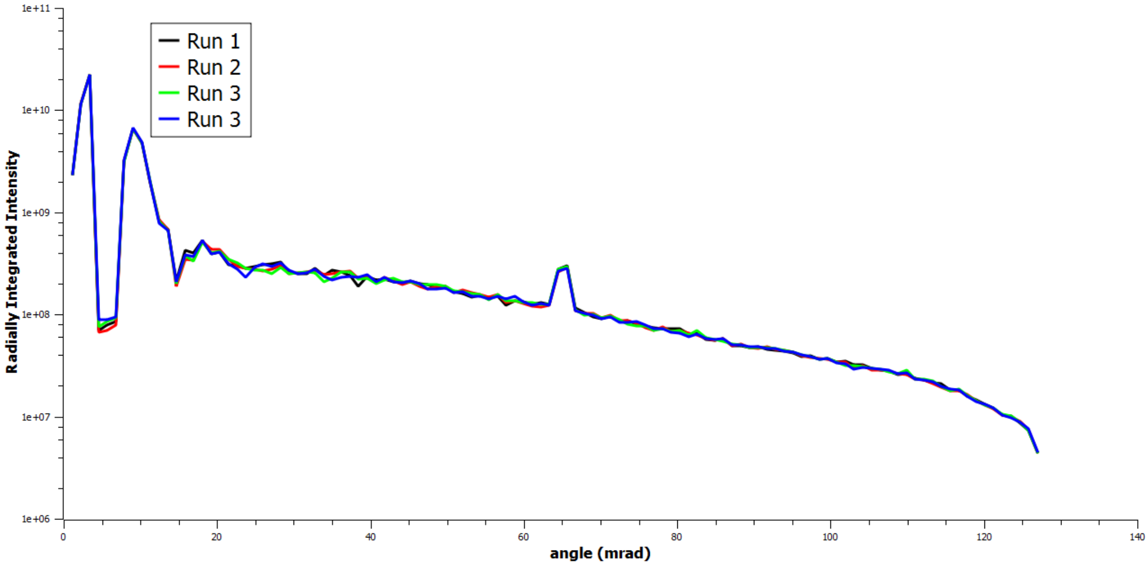

Figure 5.2: Radially integrated intensity of four identical simulations of [111] silicon at 300 KeV using the unbounded potential formulation. The observed variation is due to the random thermal motions of the atoms.

The coefficient of variance (also known as the relative standard deviation), enables quantization of the variation exhibited in Figure 5.2. Defining μ and σ as the mean and standard deviation of a given quantity respectively, the coefficient of variance, c_v, is given as:

$$c_v = \frac{\sigma}{\mu} \tag{5.1}$$

Applying equation 5.1 to each point of Figure 5.1, the average coefficient of variance, $\bar{c_v}$, is found to be $\bar{c_v} = 0.0327$. The results presented in the subsequent sections compare only two runs, so $\bar{c_v} = 0.0327$ may not be ideally representative of the variance levels encountered in subsequent sections. If the coefficient of variance is calculated Runs 1 and 2 in Figure 5.2 instead, the coefficient of variance is found to be $\bar{c_v} = 0.0287$.

Since all of the simulations plotted in Figure 5.2 were initialized with identical starting conditions, any two simulation with an average coefficient of variance below $\bar{c_v} \approx 0.03$ are essentially indistinguishable.

5.3 Kirkland versus Peng Parameterization

In Chapter 4 the Kirkland and Peng potential parameterizations were introduced. It was argued that since the corresponding electron scattering factors were parameterized to $q = 12$ Å^{-1}, there should be little variation between simulations using the Kirkland and Peng potentials provided that both sets of simulations use either the bounded or unbounded formulation.

In this chapter, the assumption of identical behaviour is tested for the case of bounded potentials using a variety of slice thicknesses at both 100 KeV and 300 KeV. As the Kirkland potentials can not be evaluated analytically between arbitrary bounds, the Kirkland potentials were integrated numerically with a maximum relative error set to 1 in 100000. Figures 5.3, 5.4 and 5.5 compare the Kirkland and Peng potentials at 100 KeV for slice thicknesses of 3.135 Å, 0.3135 Å and 0.1045 Å respectively. Figures 5.6, 5.7 and 5.8 compare the Kirkland and Peng potentials at 300 KeV for slice thicknesses of 3.135 Å, 0.3135 Å and 0.1045 Å, respectively.

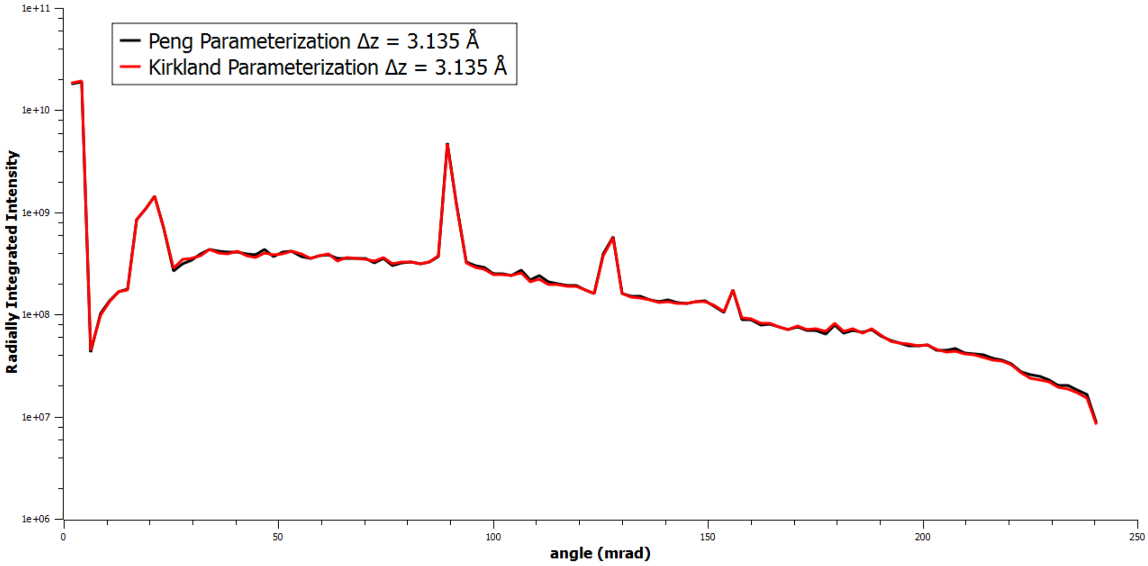

Figure 5.3: Radially integrated intensity of two simulations of [111] silicon at 100 KeV using the bounded potential formulation for both the Peng and Kirkland potential parameterizations. The average coefficient of variance between these two simulations was determined to be $\bar{c_v} = 0.0203$.

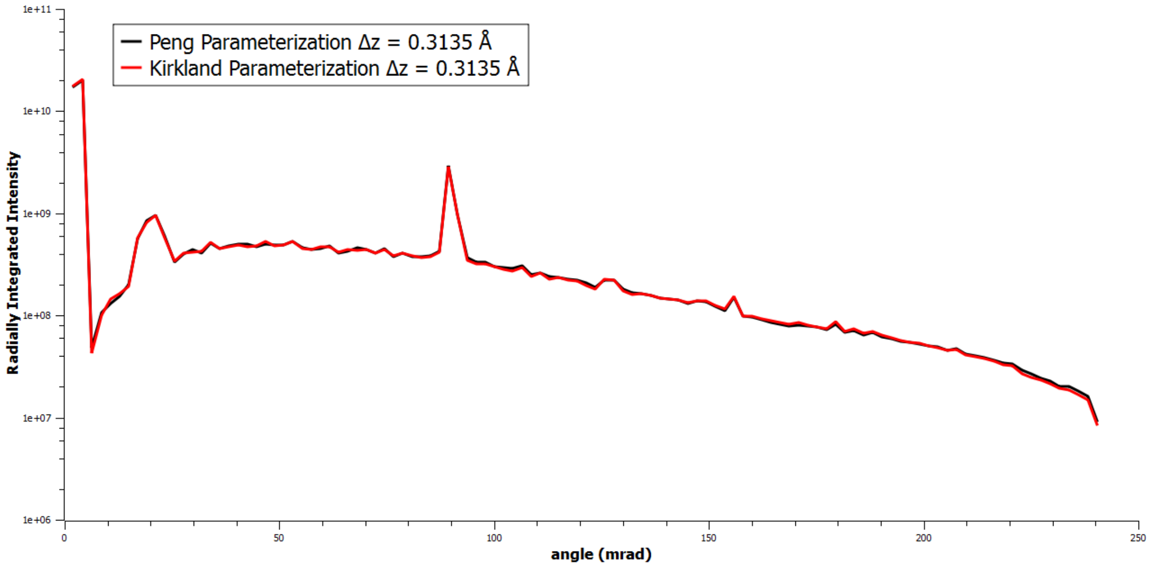

Figure 5.4: Radially integrated intensity of two simulations of [111] silicon at 100 KeV using the bounded potential formulation for both the Peng and Kirkland potential parameterizations. The average coefficient of variance between these two simulations was determined to be $\bar{c_v} = 0.0214$.

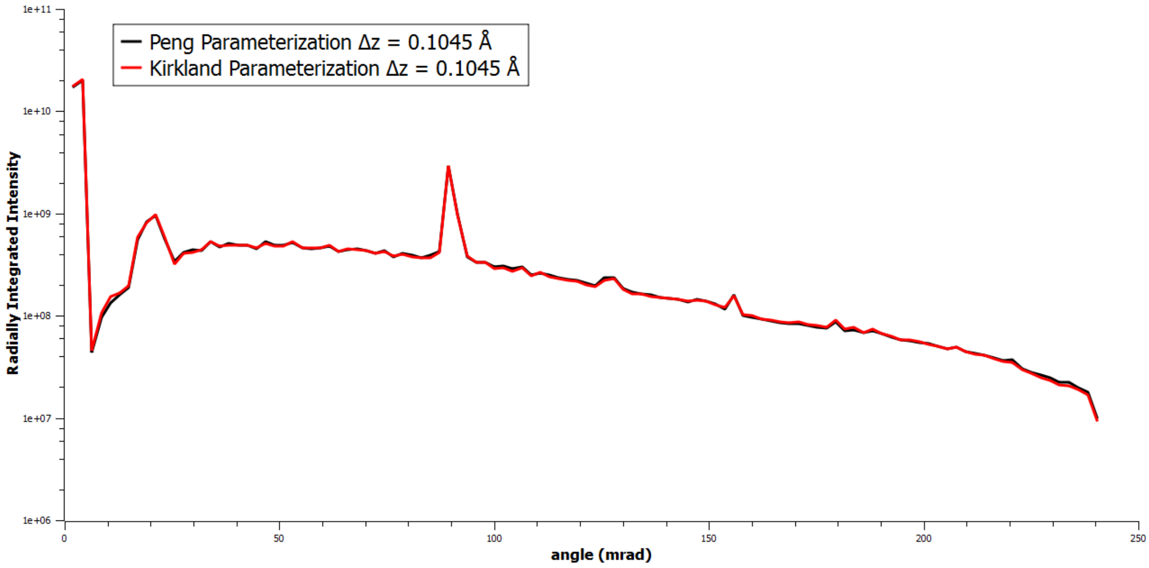

Figure 5.5: Radially integrated intensity of two simulations of [111] silicon at 100 KeV using the bounded potential formulation for both the Peng and Kirkland potential parameterizations. The average coefficient of variance between these two simulations was determined to be $\bar{c_v} = 0.0194$.

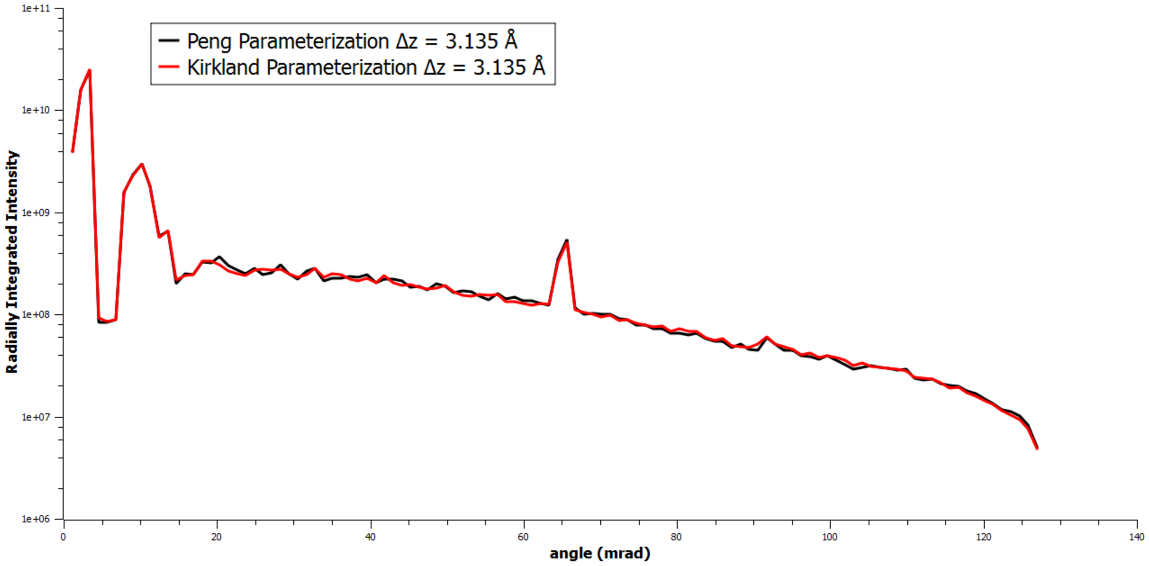

Figure 5.6: Radially integrated intensity of two simulations of [111] silicon at 300 KeV using the bounded potential formulation for both the Peng and Kirkland potential parameterizations. The average coefficient of variance between these two simulations was determined to be $\bar{c_v} = 0.0343$.

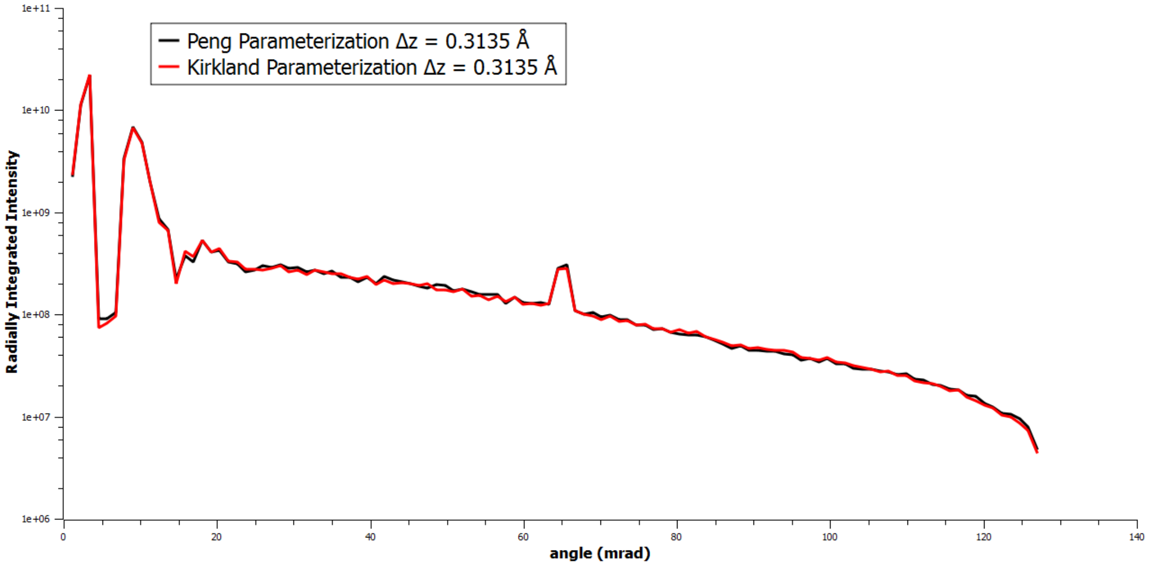

Figure 5.7: Radially integrated intensity of two simulations of [111] silicon at 300 KeV using the bounded potential formulation for both the Peng and Kirkland potential parameterizations. The average coefficient of variance between these two simulations was determined to be $\bar{c_v} = 0.0318$.

The Peng and Kirkland potential parameterizations plotted in Figures 5.3 through 5.8 compare favourably with one another with coefficients of variation typically around $\bar{c_v} =$

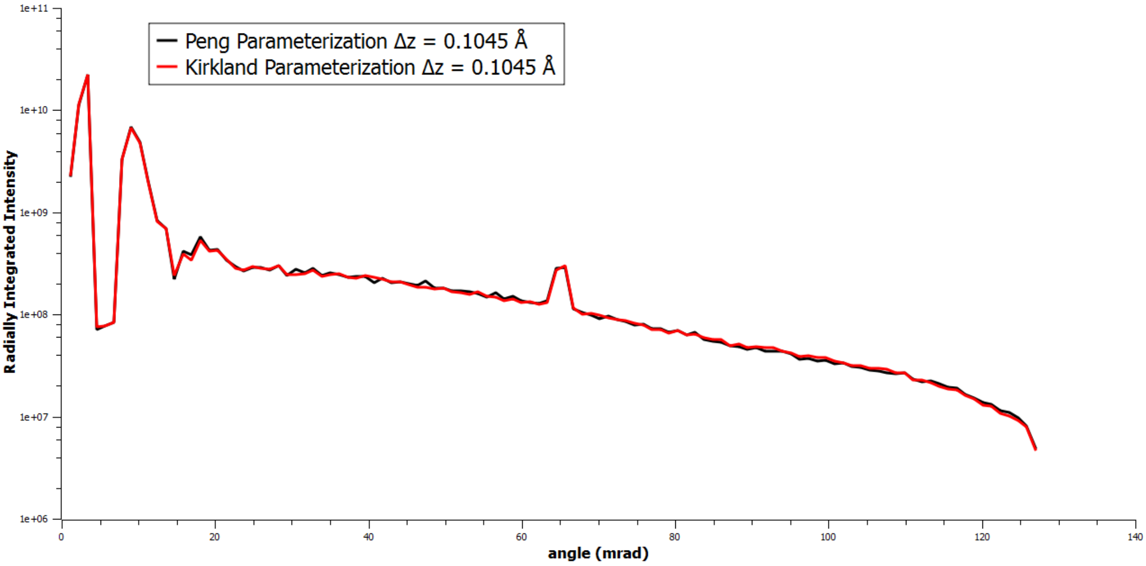

Figure 5.8: Radially integrated intensity of two simulations of [111] silicon at 300 KeV using the bounded potential formulation for both the Peng and Kirkland potential parameterizations. The average coefficient of variance between these two simulations was determined to be $\bar{c_v} = 0.0265$.

0.02 or $\bar{c_v} = 0.03$. Hence there is little difference in using the Peng or Kirkland potential parameterizations other than the time required for evaluation, with the numeric integration typically being much slower than the analytic evaluation.

5.4 Unbounded Potentials versus Bounded Potentials

According to Kirkland, due to the unbounded nature of the atomic potential calculation, the multislice solution is only accurate at slice thicknesses greater than $\Delta z \approx 1.0$ Å [4]. In this section, this hypothesis is tested through the simulation of [111] silicon using both Kirkland's formulation of the potential and the unbounded formulation developed in Chapter 4. Figures 5.9 and 5.10 plot radially integrated intensities for a series of bounded simulations at 100 KeV and 300 KeV, respectively.

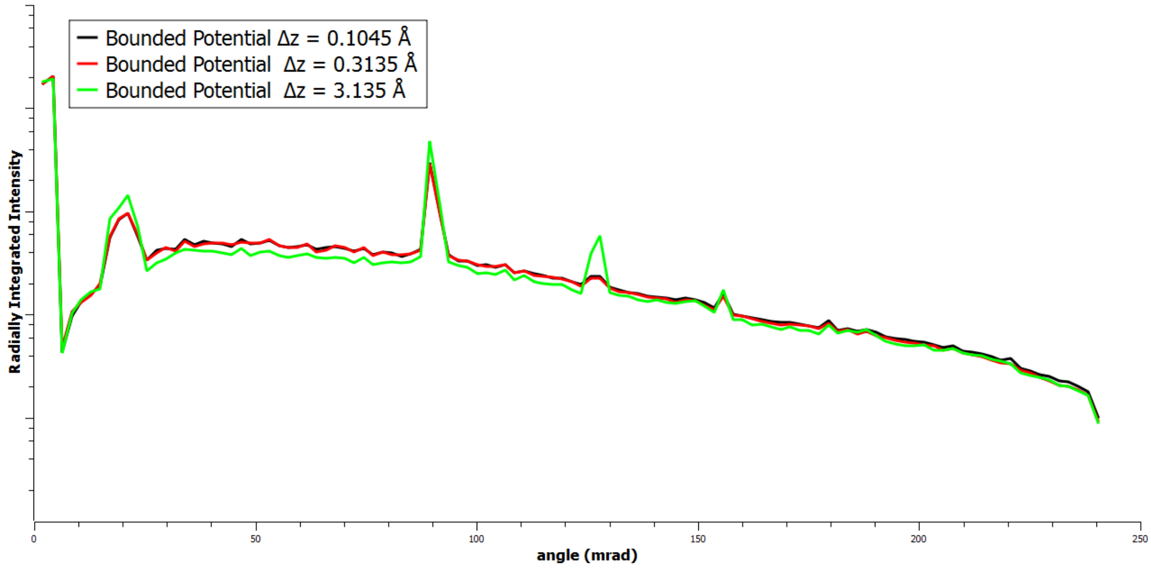

Figure 5.9: Radially integrated intensity of three simulations of [111] silicon at 100 KeV using the bounded potential formulation. Note that both the $\Delta z = 0.1045$ Å and $\Delta z = 0.3135$ Å appear to be nearly convergent with $\bar{c}_v = 0.0247$. In addition, note that the intensity of the SOLZ is significantly reduced in the $\Delta z = 0.1045$ Å and $\Delta z = 0.3135$ Å simulations compared to the $\Delta z = 3.135$ Å simulation.

Since the multislice method with bounded potentials becomes more accurate as the slice thickness decreases, the $\Delta z = 0.1045$ Å simulations shown in Figures 5.9 and 5.10 should be more accurate than either the $\Delta z = 0.3135$ Å or $\Delta z = 3.135$ Å simulations. Examining Figures 5.9 and 5.10, it is observed that the $\Delta z = 3.135$ Å simulations overestimate the magnitude of the higher order Laue zones (HOLZ). Hence, simulations with $\Delta z \approx 3$ Å will show features which are not present in more accurate simulations.

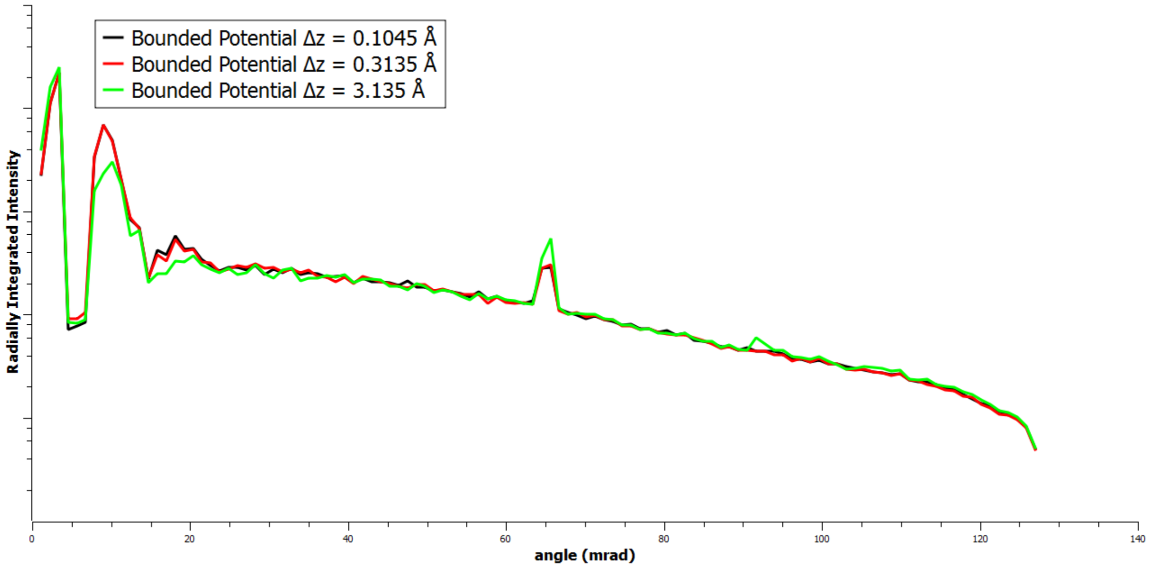

Figure 5.10: Radially integrated intensity of three simulations of [111] silicon at 300 KeV using the bounded potential formulation. Note that both the $\Delta z = 0.1045$ Å and $\Delta z = 0.3135$ Å appear to be nearly convergent with $\bar{c_v} = 0.0288$. In addition, note that the magnitude of both the FOLZ and SOLZ are significantly reduced in the $\Delta z = 0.1045$ Å and $\Delta z = 0.3135$ Å simulations compared to the $\Delta z = 3.135$ Å simulation.

Desiring to test the validity of Kirkland's minimum slice thickness hypothesis for the case of unbounded potentials, a series of simulations were run with $\Delta z < 1.0$ Å. Figures 5.11, 5.12, 5.13 and 5.14 plot comparisons of bounded and unbounded 300 KeV simulations for slice thicknesses of $\Delta z = 3.135$ Å, $\Delta z = 0.3135$ Å, $\Delta z = 0.1045$ Å and $\Delta z = 0.01045$ Å, respectively.

Examining Figures 5.11, 5.12, 5.13 and 5.14 and noting that for each comparison $\bar{c_v} \approx 0.03$, it is evident that the difference between the bounded potential and unbounded potential formulations in the multislice method becomes small as the slice thickness decreases. However, it is possible that the similarities between the formulations are due in some way to random thermal vibrations blurring out the differences between the methods. To test this, several additional simulations were run without thermal vibrations. Figures 5.15, 5.16, 5.17 and 5.18 plot comparisons of bounded and unbounded 300 KeV simulations without thermal vibrations for slice thicknesses of $\Delta z = 3.135$ Å, $\Delta z = 1.045$ Å, $\Delta z = 0.3483$ Å and $\Delta z = 0.1161$ Å, respectively.

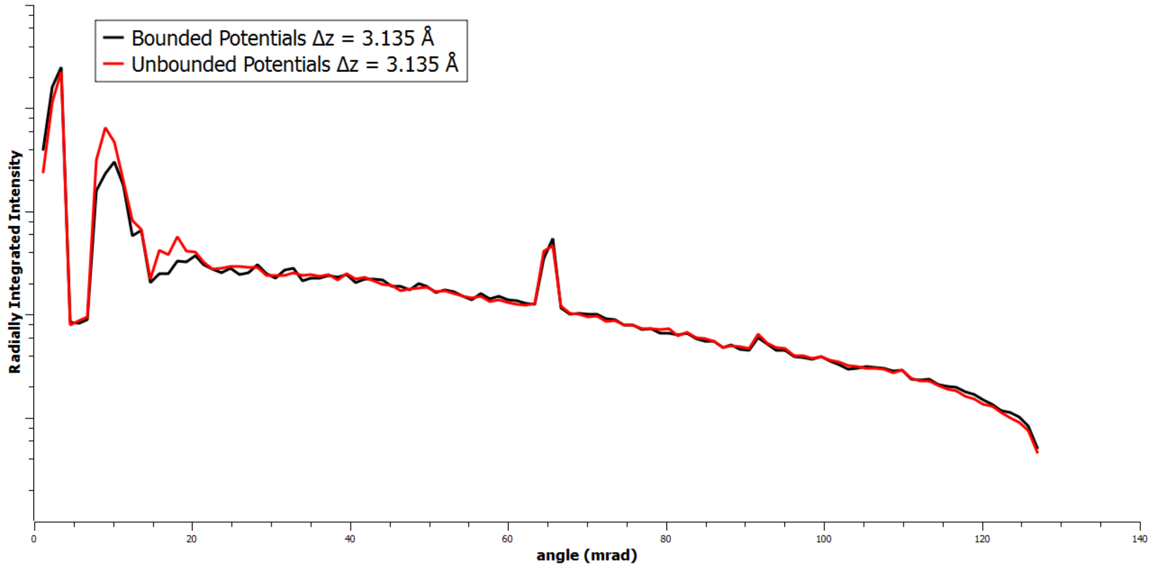

Figure 5.11: Radially integrated intensity of [111] silicon at 300 KeV for both the bounded and unbounded potential formulations. At $\Delta z = 3.135$ Å, there is a significant difference between the bounded and unbounded potential formulations.

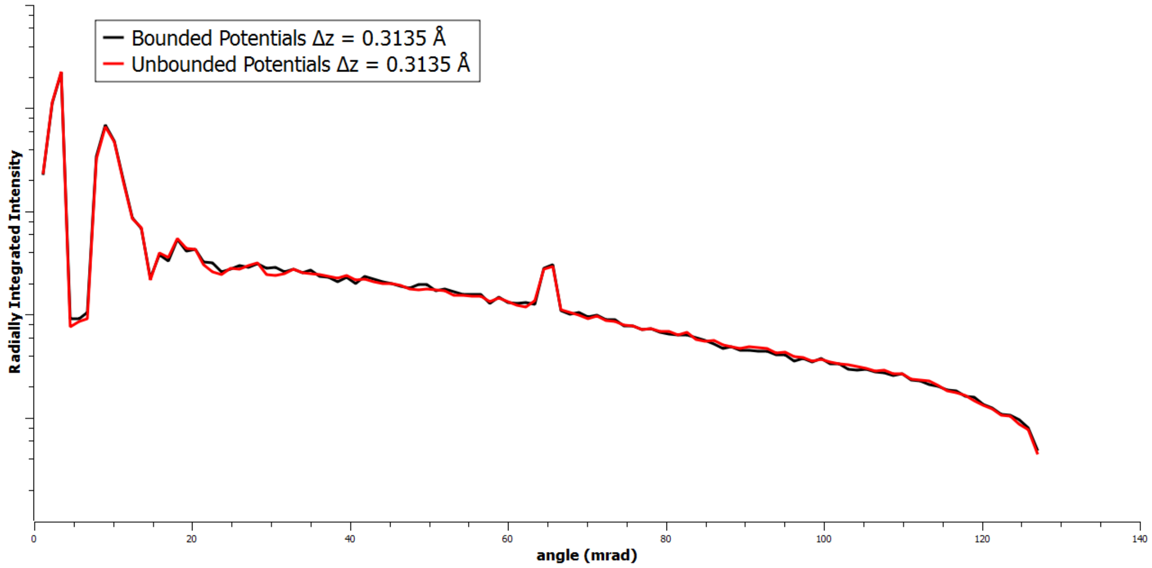

Figure 5.12: Radially integrated intensity of [111] silicon at 300 KeV for both the bounded and unbounded potential formulations. The simulations for bounded and unbounded potential formulations agree very well with $\bar{c}_v = 0.0339$. It should be noted however, that between 4 mrad and 8 mrad and the coefficient of variation is considerably higher ($c_v \approx 0.09$).

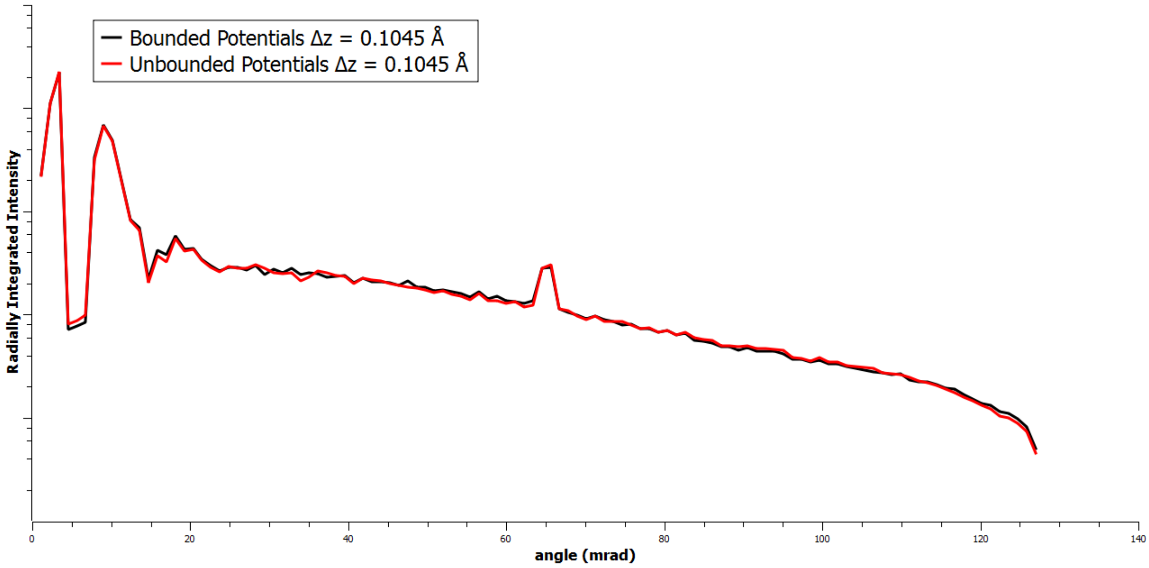

Figure 5.13: Radially integrated intensity of [111] silicon at 300 KeV for both the bounded and unbounded potential formulations. The simulations for bounded and unbounded potential formulations agree very well with $\bar{c_v} = 0.0344$. It should be noted however, that between 4 mrad and 8 mrad and again at about 17 mrad the coefficient of variation is $c_v \approx 0.11$.

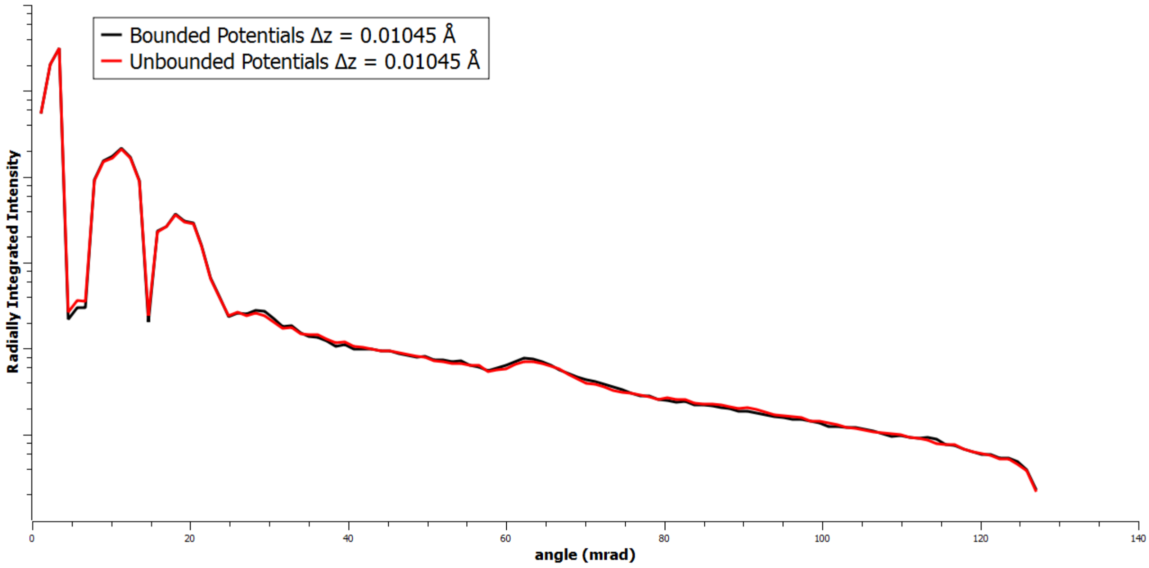

Figure 5.14: Radially integrated intensity of [111] silicon at 300 KeV for both the bounded and unbounded potential formulations. Due to the small slice thickness of $\Delta z = 0.01045$ Å, running the full 500 Å simulation would have been prohibitively time consuming, so the simulation was instead run for 50 Å. The simulations for bounded and unbounded potential formulations agree very well with $\bar{c_v} = 0.0322$. It should be noted however, that between 4 mrad and 8 mrad and again at about 15 mrad the coefficient of variation is $c_v \approx 0.12$.

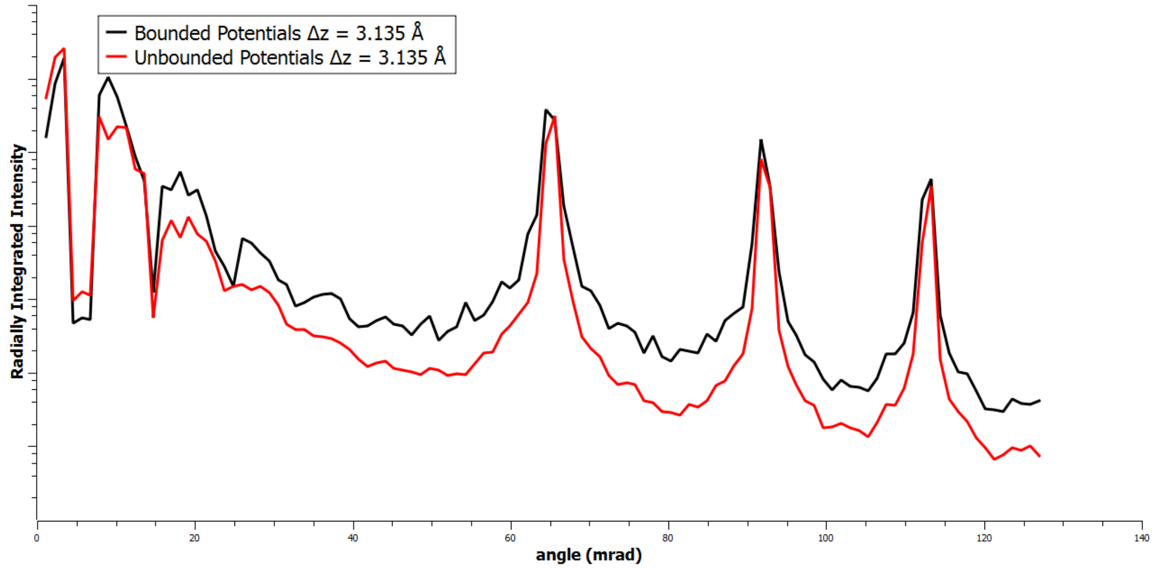

Figure 5.15: Radially integrated intensity of [111] silicon at 300 KeV for both the bounded and unbounded potential formulations with no thermal effects. The simulations for bounded and unbounded potential formulations are in poor agreement on average with $\bar{c}_v = 0.7776$.

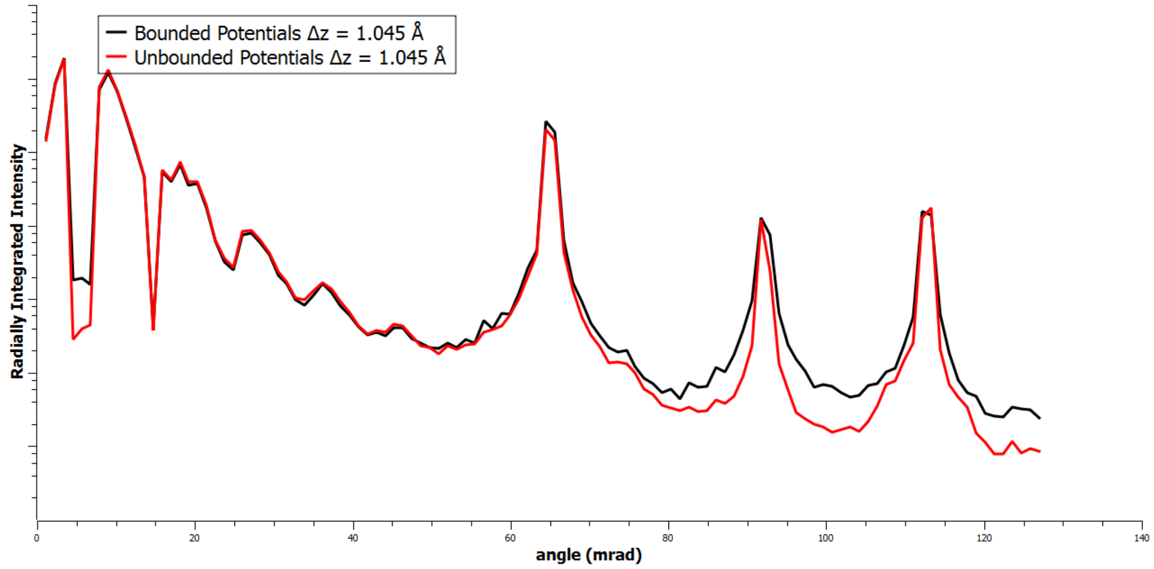

Figure 5.16: Radially integrated intensity of [111] silicon at 300 KeV for both the bounded and unbounded potential formulations with no thermal effects. The simulations for bounded and unbounded potential formulations are in poor agreement on average with $\bar{c}_v = 0.3158$.

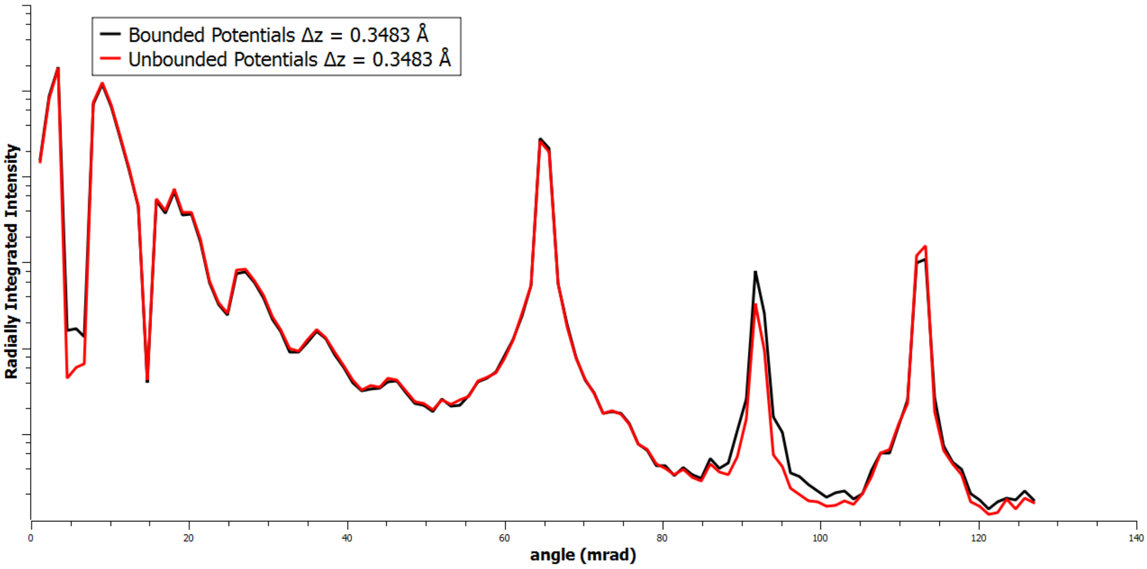

Figure 5.17: Radially integrated intensity of [111] silicon at 300 KeV for both the bounded and unbounded potential formulations with no thermal effects. The simulations for bounded and unbounded potential formulations are in fairly poor agreement with $\bar{c}_v = 0.1092$. It should be noted that between 4 mrad and 8 mrad the coefficient of variation is $c_v \approx 0.66$.

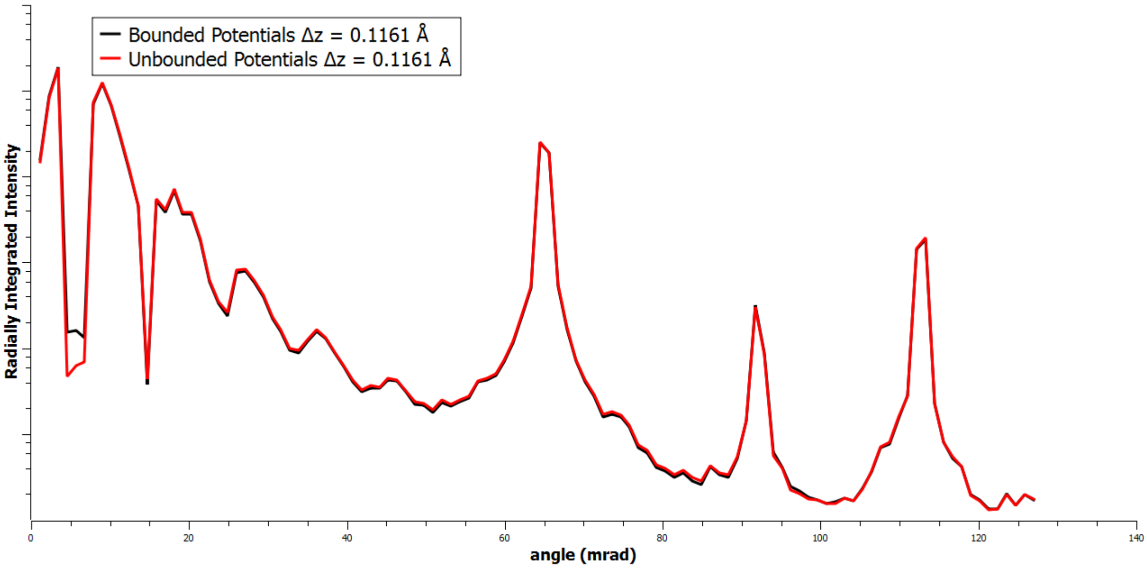

Figure 5.18: Radially integrated intensity of [111] silicon at 300 KeV for both the bounded and unbounded potential formulations. The simulations for bounded and unbounded potential formulations are in fairly good agreement on average with $\bar{c}_v = 0.0476$. For angles greater than 20 mrad $\bar{c}_v = 0.0319$, but between 4 mrad and 8 mrad and again at about 15 mrad the coefficient of variation is $c_v \approx 0.48$.

The consistent overestimation of the trough between between 4 mrad and 8 mrad by the unbounded potential formulation (shown in Figures 5.15, 5.16, 5.17 and 5.18) demonstrates that the two potential formulations do not fully converge as the slice thickness decreases. However, as shown in Figures 5.19 and 5.20, the unbounded potential formulation most accurately approximates the bounded potential formulation when the slice thickness is made small. Hence, the hypothesis that the multislice method with unbounded potentials is accurate for only $\Delta z > 1$ Å does not necessarily hold true. Although the unbounded potential formulation does not converge perfectly to the bounded potential formulation, the variation becomes smaller as the slice thickness is decreased.

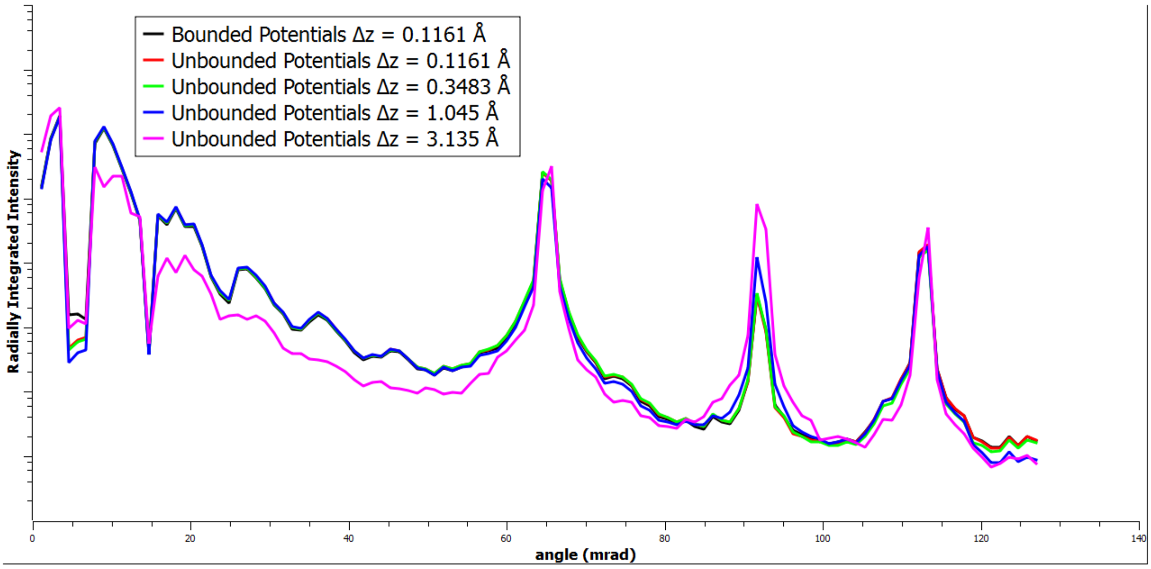

Figure 5.19: Radially integrated intensity of [111] silicon at 300 KeV for the bounded potential formulation with $\Delta z = 0.1161$ Å and each of the unbounded potential formulations simulations plotted in Figures 5.15 through 5.18. As the slice thickness is decreased, the unbounded potential formulations closely approach the bounded potential formulation. Since the multislice method with bounded potential formulation becomes more accurate as the slice thickness is decreased, the simulation with $\Delta z = 0.1161$ Å is the most accurate of the unbounded simulations run and serves as a reference solution. Since the unbounded potential formulation approaches the reference solution as the slice thickness is decreased, the hypothesis that the multislice method with unbounded potential formulation is only accurate when $\Delta z > 1$ Å does not necessarily hold true.

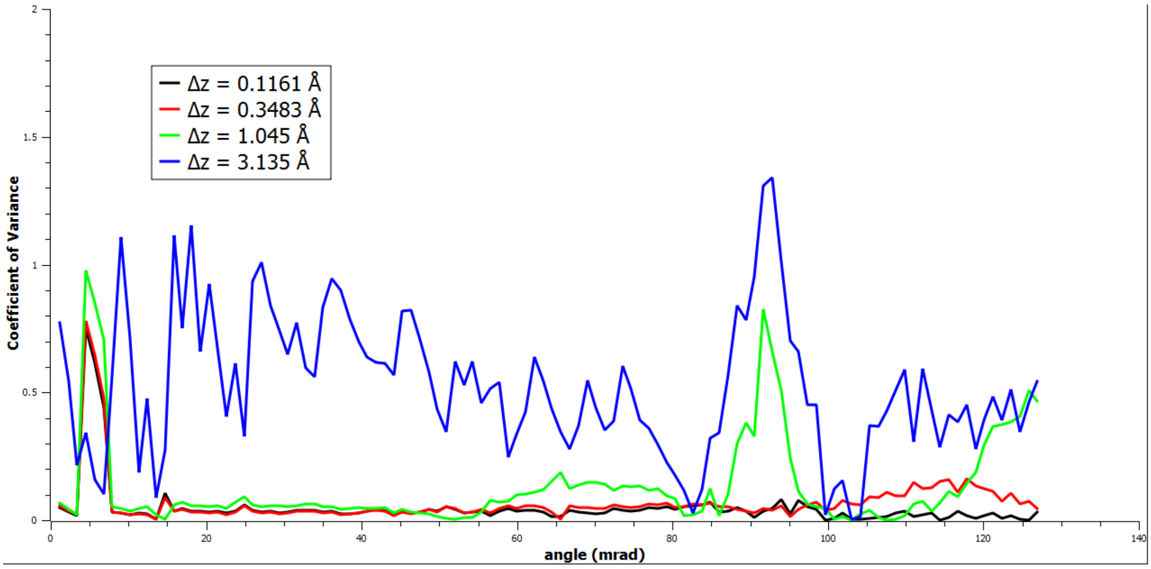

Figure 5.20: Coefficient of variance between the bounded potential formulation with $\Delta z =$ 0.1161 Å and each of the unbounded potential formulations simulations plotted in Figures 5.15 through 5.18. The average coefficients of variance, $\bar{c_v}$, were determined to be 0.0476, 0.0695, 0.1314 and 0.5236 respectively.

5.5 Multislice versus RK4

Desiring to determine what effects, if any, were caused by neglecting the contribution of the second derivative term in z, a RK4 integrator was written to solve equation 2.6. Due to the fact that the RK4 integrator was found to be stable for only very small slice thicknesses ($\Delta z \lesssim 0.005$ Å), running the full 500 Å simulation would have been prohibitively time consuming. Instead, the simulation was instead run for 28.215 Å. The data presented in this section was taken from the 25.08 Å slices of the simulations. Figures 5.21 and 5.22 plot comparisons between the unbounded and bounded potential formulation of the multislice method at 300 KeV for silicon. The slice thicknesses for Figures 5.21 and 5.22 were $\Delta z = 0.003135$ Å and $\Delta z = 0.0003135$ Å respectively.

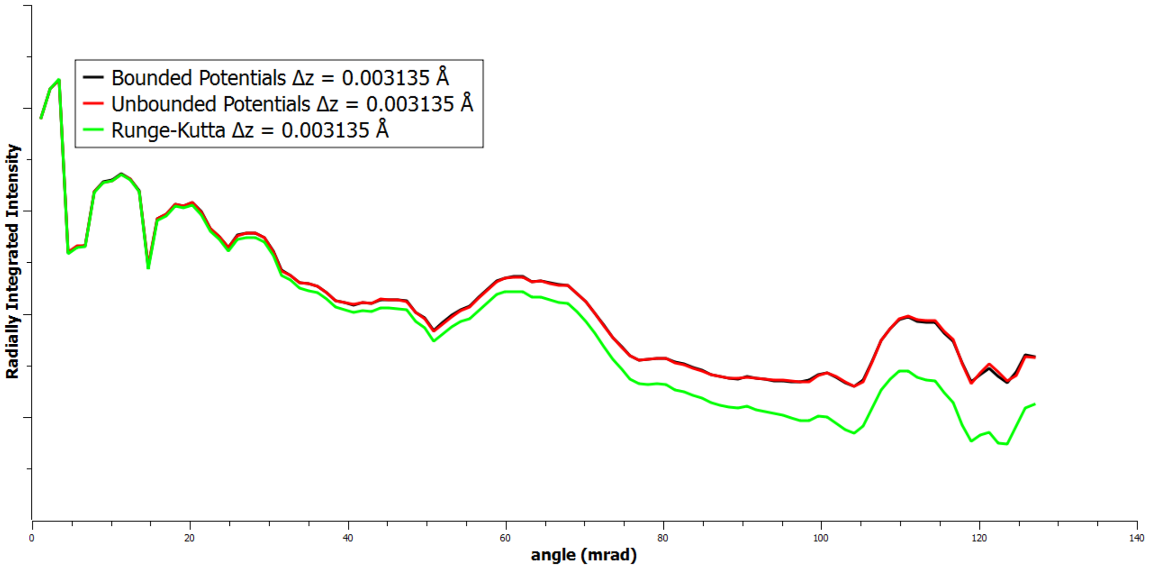

Figure 5.21: Runge-Kutta, bounded multislice and unbounded multislice simulations of 300 KeV [111] silicon for $\Delta z = 0.003135$ Å. At high angles it is observed that the Runge-Kutta simulation deviates substantially from the multislice simulation. The average coefficient of variance between the multislice simulations was determined to be $\bar{c}_v = 0.0216$, reinforcing the earlier observation that as the slice thickness is made small, the unbounded and bounded potential formulations tend to converge.

Figures 5.21 and 5.22 indicate that the Runge-Kutta method deviates fairly substantially from the multislice methods at high angles, while Figure 5.23 demonstrates that the Runge-Kutta method is quickly convergent. Although the multislice methods reproduces all of the same features of the Runge-Kutta method, the scaling of these features appears to be sub-

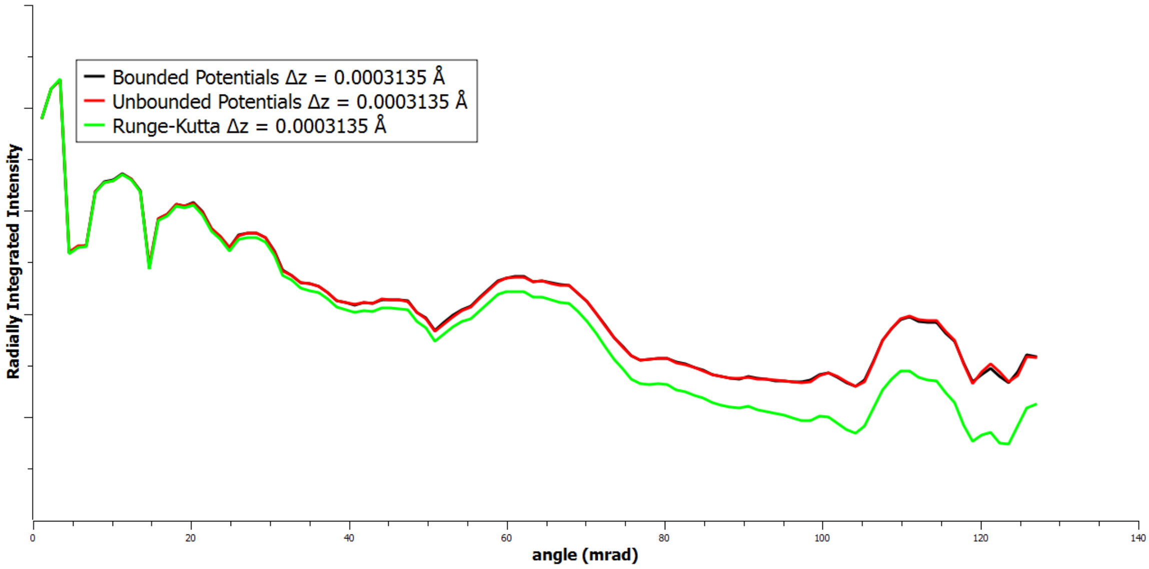

Figure 5.22: Runge-Kutta, bounded multislice and unbounded multislice simulations of 300 KeV [111] silicon for $\Delta z = 0.003135$ Å. At high angles it is observed that the Runge-Kutta simulation deviates substantially from the multislice simulation. The average coefficient of variance between the multislice simulations was determined to be $\bar{c_v} = 0.0213$, reinforcing the earlier observation that as the slice thickness is made small, the unbounded and bounded potential formulations tend to converge.

stantially different. Therefore, if the Runge-Kutta method is representative of the actual physical process the electrons undergo as they diffract through the specimen, the multislice method may not be the ideal simulation to compare with experiment (for additional information see Rother [1]).

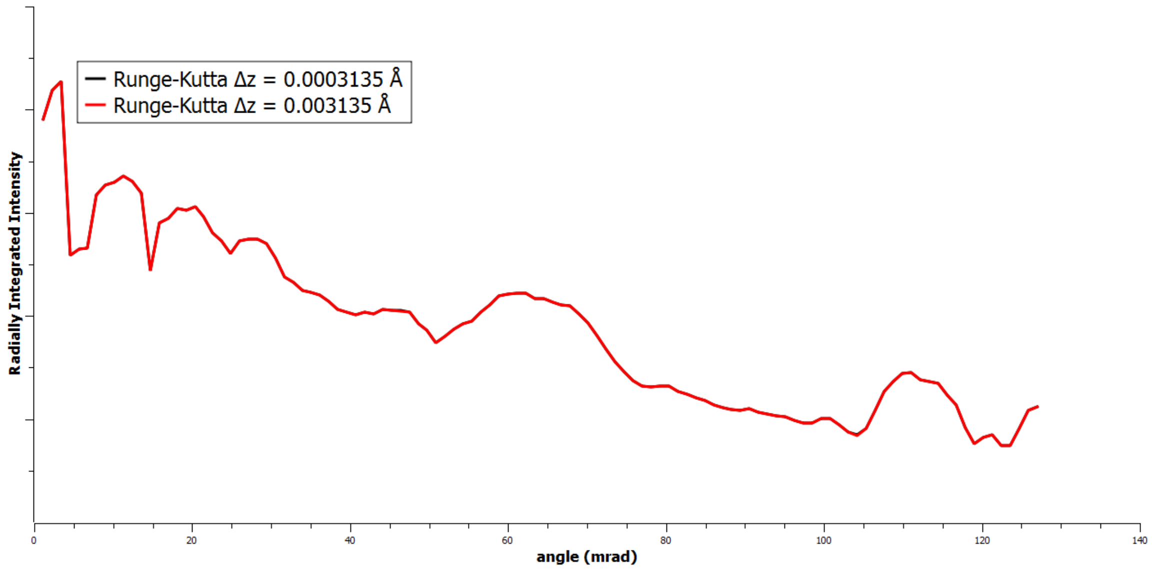

Figure 5.23: Runge-Kutta simulations of 300 KeV [111] silicon for $\Delta z = 0.003135$ Å and $\Delta z = 0.0003135$ Å. The average coefficient of variance between the two simulations was determined to be be $\bar{c_v} = 0.0006$, indicating that the RK4 method converges quickly as expected.

5.6 Effects of super cell Size

Implicit in the multislice solution is the assumption that the sample can be accurately modeled through the use of periodic boundary conditions. However, although it is true that the sample can be considered periodic in many cases (for the case of non-periodic, defected samples see Kirkland [4]), the wave function should almost certainly never be.

When a discrete Fourier transform (or other process assuming periodic boundary conditions) is used to evaluate derivatives and convolutions, the functions in question can be effectively considered as tiling all of space as in Figure 5.24. Any portion of the initial wave function that "crosses" the super cell boundaries is reinstated at the opposite side of the cell with the same orientation (alternatively one can consider the reinstated wave function to be from a neighbouring super cell). This means that any portion of the wave function that would normally spread out throughout the specimen beyond the borders of the super cell will instead remain confined within the super cell.

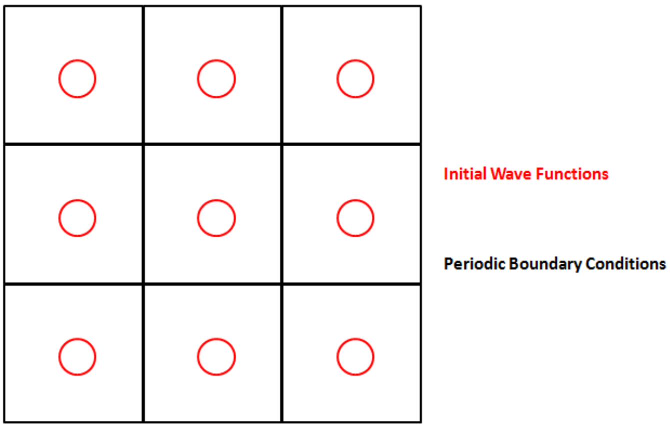

Figure 5.24: Applying periodic boundary conditions is equivalent to tiling the finite size initial conditions throughout all space. Any portion of the wave function that would normally spread out throughout the specimen beyond the borders of the super cell will instead remain confined within the super cell due to the action of the neighbouring wave functions in each tile.

If the evolution of the wave function depended only on the specimen potential, one would expect the CBED pattern, as an image of the reciprocal space wave function, to remain unaffected while the real space image would show substantial deviation from experimental results. However, the evolution of the wave function does not simply depend on the local specimen potential but also on the local curvature of the wave function.

Since applying periodic boundary conditions prevents the wave function from spreading out throughout the sample, the curvature of a wave function confined within a super cell will be different than one permitted to spread out throughout the sample. As such, the wave functions may evolve substantially differently in the two cases.

Figure 5.25 shows the effect of different super cell sizes on the radially integrated intensity of a CBED pattern. The simulations presented earlier in the chapter were run with super cell dimensions of $x = 23.0376$ Å and $y = 26.6014$ Å corresponding to a 3x2 tiling of the rectangular silicon unit cell. The plots shown in Figure 5.25 were each simulated using different sized silicon super cells as indicated in the legend. In order to maintain the same angular dependance in each of the simulation, the image size was scaled accordingly; 1x1 simulations were run at 512x512 pixels while 2x2 simulations were run at 1024x1024 pixels and so on.

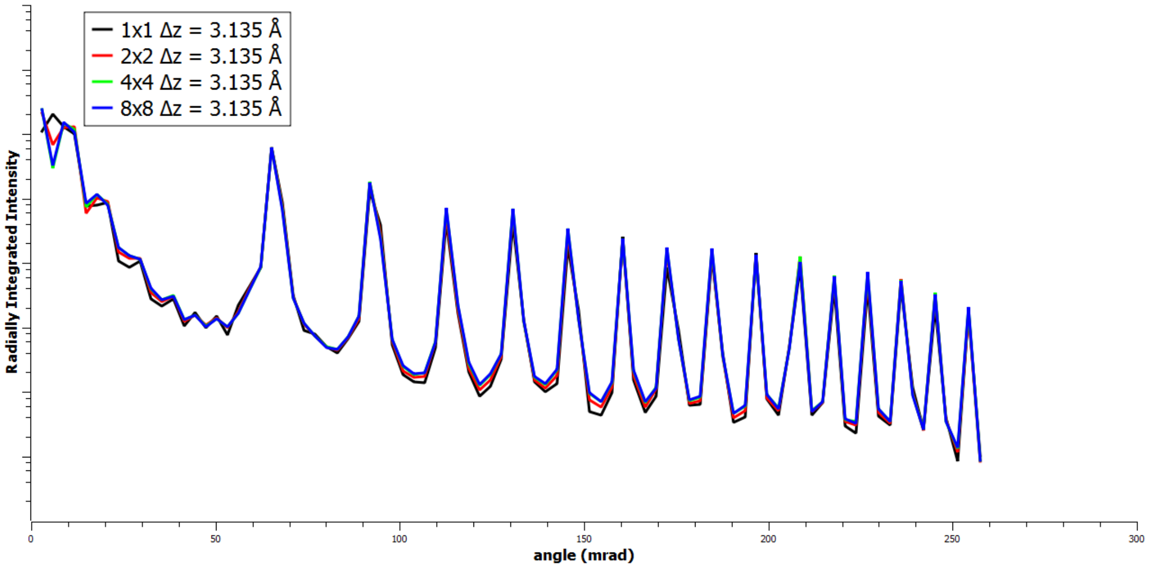

Figure 5.25: Radially integrated intensity of [111] silicon at 300 KeV for various super cell sizes as indicated in the legend. In these simulations, the unbounded potential formulation of the multislice method was used for the sake of computational efficiency. The simulations themselves are in fairly poor agreement with one another ($\bar{c_v} \approx 0.10$) with one exception; between the 4x4 and 8x8 simulations $\bar{c_v} = 0.0190$

In Figure 5.25, the majority of the simulations are in fairly poor agreement with one another (between the 1x1 and 8x8 simulation, $\bar{c_v} = 0.1949$). The exceptions to this are the 4x4 and 8x8 runs, indicating that at these sizes the super cells are large enough that the distortion due to periodic boundary conditions in minimal. Despite the majority of the simulations being in poor agreement with one another, Figure 5.25 demonstrates that each of the simulations reproduces the same basic features with similar intensities (the 1x1 simulation is an exception to this with an additional low angle maximum). The same cannot be said for the real space images of those respective simulations.

Figure 5.26 shows the effect of different super cell sizes on the radially integrated intensity of real space patterns. These patterns were formed by Fourier transforming the wave functions used to generate the plots in Figure 5.25 to real space.

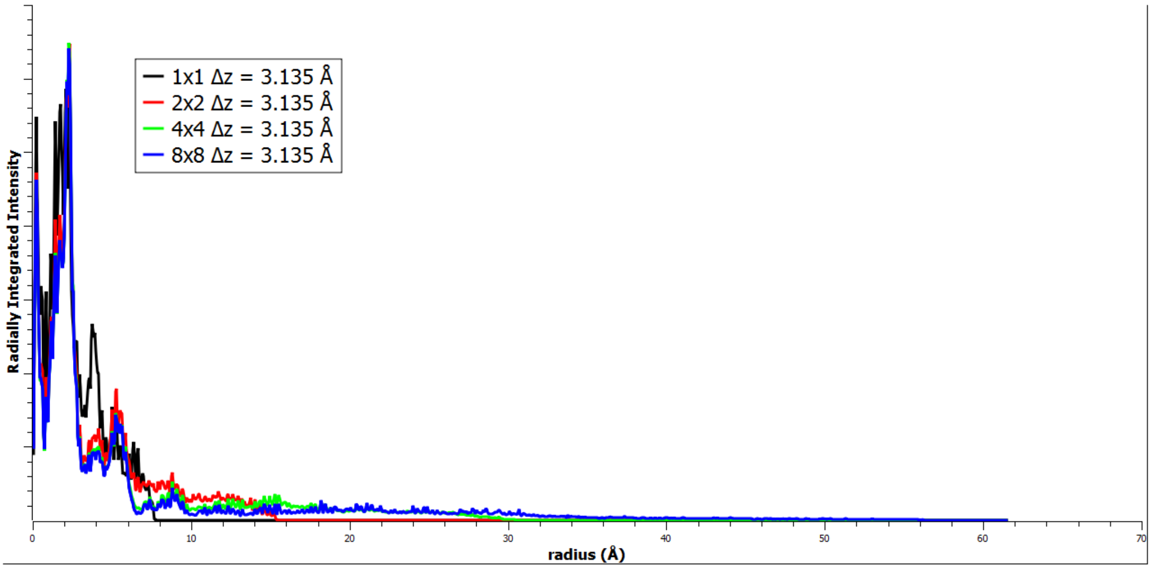

Figure 5.26: Radially integrated real space intensity of [111] silicon at 300 KeV for various super cell sizes as indicated in the legend. In these simulations, the unbounded potential formulation of the multislice method was used for the sake of computational efficiency and the image was centered at the location of the CBED probe. The simulations themselves are in fairly poor agreement with one another between $r = 0$ Å and $r = 7$ Å ($\bar{c_v} \approx 0.23$) with one exception; between the 4x4 and 8x8 simulations $\bar{c_v} = 0.0520$. Note that unlike other plots in this chapter, the y axis has not been log scaled.

From Figure 5.26, it can be observed that there are significant differences in the real space images formed by simulations of different super cell sizes. Even between the 4x4 and

8x8 plots there some deviation at small radii ($\bar{c_v} = 0.0520$) which becomes increasingly pronounced at larger radii. The 1x1 image is observed to have intensity maxima that are entirely absent in the other simulations and those maxima it shares with the other simulations are often shifted.

To give a better idea of the differences between the real space images plotted in 5.26, the total radially integrated intensity of each of the simulations is plotted in Figure 5.27 as a function of radius.

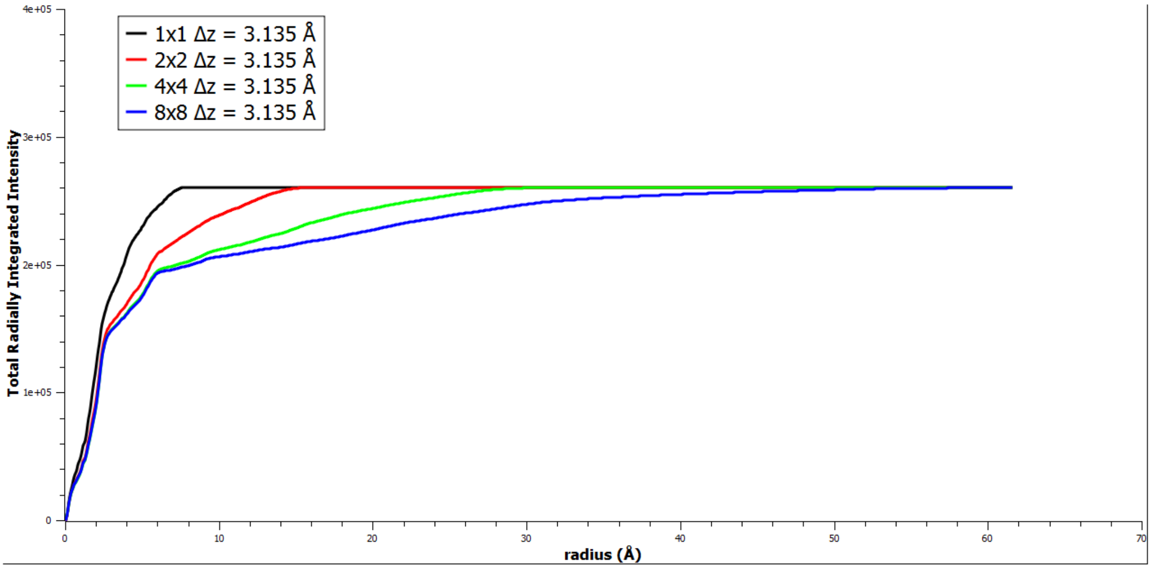

Figure 5.27: Total radially integrated real space intensity plotted as a function of radius. As with Figure 5.26, the plots are of [111] silicon at 300 KeV for various super cell sizes as indicated in the legend. In these simulations, the unbounded potential formulation of the multislice method was used for the sake of computational efficiency and the image was centered at the location of the CBED probe.

Figure 5.27 demonstrates that as the super cell is made larger, more of the intensity is found further away from the initial probe. Figures 5.25, 5.26 and 5.27 indicate that using a small super cell can cause a significant amount of distortion and may lead to erroneous results. For this reason, it is preferable to use a larger super cell whenever possible.

This result is particularly relevant as all of the simulation in the previous sections of the chapter were run using a 3x2 super cell. Examination of Figures 5.25, 5.26 and 5.27 indicates that simulations using a 3x2 unit cell would not be fully convergent on the non-periodic case for 500 Å simulations. As such, future simulations should be run using significantly larger super cells to reduce this source of error.

Chapter 6

Conclusions

6.1 Summary of Results

In Chapter 5 it was demonstrated that, although the unbounded and bounded formulations of the potential did not converge completely, using a smaller slice thickness for the unbounded potential formulation nevertheless produced more accurate results. These findings indicate that the minimum slice thickness hypothesis made made by Kirkland [4], may not be correct.

Comparisons between simulations using the multislice method and simulation of equation 2.6 using Runge-Kutta methods indicate that there is a substantial difference between the two methods. If the Runge-Kutta method is in fact the more physically accurate simulation, this indicates that the multislice method can show substantial deviations from physically accurate results. Interestingly it was found that both the bounded and unbounded formulations of the multislice method produced equally deviant results.

Finally, it was demonstrated the the dimensions of the super cell can play a significant role in the formation of both real space and CBED (reciprocal space) patterns. It was suggested that future simulations should take this effect into consideration by using an artificially large super cell to simulate the non-periodic case.

6.2 Recommendations for Future Work

Future work should concentrate on first establishing an accurate simulation method by which the other simulations can be judged. For the work presented in this thesis, the RK4 method was used to this end. However, it should be stressed that no independent verification of the correctness of the code or accuracy of the simulation was performed for the RK4 method. As such, all results pertaining to the RK4 method should be reexamined in the future.

Once a more accurate method is established, the differences between the various methods could be more accurately quantified and a maximally efficient (in terms of accuracy versus computation time) method could be developed. Of particular interest is the wave solution presented which is both unconditionally stable and includes the contributions from the second derivative term in equation 2.6.

Appendix A

Simulation Conditions

The input file (haadf.xyz) for [111] silicon at 100 KeV using CM30 conditions is:

```
One unit cell of 111 silicon.
Type the x, y and z lattice parameters in Angstroms below.
7.6792 13.3007 9.4050
Number of times the unit cell is replicated in x, y and z directions.
3 2 54
X and Y dimensions for HAADF image.
1 1
Average defocus(angstroms), Standard deviation of defocus (angstroms), Defocus
delta (angstroms).
645 10.0 2.0
Spherical aberration coefficient (C3) in mm.
2.0
Fifth order aberration coefficient (C5) in mm.
0.0
Objective or condensor aperture in millirads.
3.1
Magnitude (angstroms) and angle (degrees) of 2-fold astigmatism.
0.0 0.0
Magnitude (angstroms) and angle (degrees) of 3-fold astigmatism.
0.0 0.0
Incident beam energy in keV.
100.0
Wavefunction size in pixels.  Must be a factor of 2for FFT algorithms to work.
512 512
Crystal tilt in the x and y directions in milliradians.
0.0 0.0
Slice thickness in angstroms.  Should be greater than about 1.0 angstroms for
```

```
a stable calculation.
3.135
Include the effects of thermal vibrations? 1 = yes, 0 = no.
1
Temperature in degrees Kelvin.
300.0
Simulation Type (1=Earl, 0=new)
0
List the atomic number, x, y and z positions of atoms in unit cell
(angstroms), and occupancy factor, thermal vibration amplitude
(angstroms).
14   5.759385   9.975547   0.000000 1.000000 0.078000
14   5.759385   9.975547   2.351259 1.000000 0.078000
14   0.000000   6.650365   0.000000 1.000000 0.078000
14   1.919795   9.975547   0.000000 1.000000 0.078000
14   0.000000   6.650365   2.351259 1.000000 0.078000
14   1.919795   9.975547   2.351259 1.000000 0.078000
14   0.000000  11.083941   3.135012 1.000000 0.078000
14   0.000000  11.083941   5.486271 1.000000 0.078000
14   3.839590   0.000000   0.000000 1.000000 0.078000
14   1.919795   3.325182   0.000000 1.000000 0.078000
14   5.759385   3.325182   0.000000 1.000000 0.078000
14   3.839590   0.000000   2.351259 1.000000 0.078000
14   1.919795   3.325182   2.351259 1.000000 0.078000
14   5.759385   3.325182   2.351259 1.000000 0.078000
14   3.839590   6.650365   0.000000 1.000000 0.078000
14   3.839590   4.433576   3.135012 1.000000 0.078000
14   1.919795   7.758759   3.135012 1.000000 0.078000
14   5.759385   7.758759   3.135012 1.000000 0.078000
14   3.839590   6.650365   2.351259 1.000000 0.078000
14   3.839590   4.433576   5.486271 1.000000 0.078000
14   1.919795   7.758759   5.486271 1.000000 0.078000
14   5.759385   7.758759   5.486271 1.000000 0.078000
14   3.839590  11.083941   3.135012 1.000000 0.078000
14   3.839590   8.867153   6.270024 1.000000 0.078000
14   1.919795  12.192335   6.270024 1.000000 0.078000
14   5.759385  12.192335   6.270024 1.000000 0.078000
14   3.839590  11.083941   5.486271 1.000000 0.078000
14   3.839590   8.867153   8.621283 1.000000 0.078000
14   1.919795  12.192335   8.621283 1.000000 0.078000
14   5.759385  12.192335   8.621283 1.000000 0.078000
14   5.759385   1.108394   3.135012 1.000000 0.078000
14   5.759385   1.108394   5.486271 1.000000 0.078000
14   5.759385   5.541971   6.270024 1.000000 0.078000
14   5.759385   5.541971   8.621283 1.000000 0.078000
14   0.000000   0.000000   0.000000 1.000000 0.078000
14   1.919795   1.108394   3.135012 1.000000 0.078000
14  -0.000000   0.000000   2.351259 1.000000 0.078000
```

```
14   1.919795   1.108394   5.486271 1.000000 0.078000
14   0.000000   4.433576   3.135012 1.000000 0.078000
14   0.000000   2.216788   6.270024 1.000000 0.078000
14   1.919795   5.541971   6.270024 1.000000 0.078000
14   0.000000   4.433576   5.486271 1.000000 0.078000
14   0.000000   2.216788   8.621283 1.000000 0.078000
14   1.919795   5.541971   8.621283 1.000000 0.078000
14   0.000000   8.867153   6.270024 1.000000 0.078000
14   0.000000   8.867153   8.621283 1.000000 0.078000
14   3.839590   2.216788   6.270024 1.000000 0.078000
14   3.839590   2.216788   8.621283 1.000000 0.078000
-1
```

The input file (haadf.xyz) for [111] silicon at 300 KeV using CM30 conditions is:

```
One unit cell of 111 silicon.
Type the x, y and z lattice parameters in Angstroms below.
7.6792 13.3007 9.4050
Number of times the unit cell is replicated in x, y and z directions.
3 2 54
X and Y dimensions for HAADF image.
1 1
Average defocus(angstroms), Standard deviation of defocus (angstroms),
Defocus delta (angstroms).
471 10.0 2.0
Spherical aberration coefficient (C3) in mm.
2.0
Fifth order aberration coefficient (C5) in mm.
0.0
Objective or condensor aperture in millirads.
3.1
Magnitude (angstroms) and angle (degrees) of 2-fold astigmatism.
0.0 0.0
Magnitude (angstroms) and angle (degrees) of 3-fold astigmatism.
0.0 0.0
Incident beam energy in keV.
300.0
Wavefunction size in pixels.  Must be a factor of 2for FFT algorithms to work.
512 512
Crystal tilt in the x and y directions in milliradians.
0.0 0.0
Slice thickness in angstroms.  Should be greater than about 1.0 angstroms for
a stable calculation.
3.135
Include the effects of thermal vibrations? 1 = yes, 0 = no.
1
Temperature in degrees Kelvin.
```

```
300.0
Simulation Type (1=Earl, 0=new)
1
List the atomic number, x, y and z positions of atoms in unit cell
(angstroms), and occupancy factor, thermal vibration amplitude
(angstroms).
14   5.759385   9.975547   0.000000 1.000000 0.078000
14   5.759385   9.975547   2.351259 1.000000 0.078000
14   0.000000   6.650365   0.000000 1.000000 0.078000
14   1.919795   9.975547   0.000000 1.000000 0.078000
14   0.000000   6.650365   2.351259 1.000000 0.078000
14   1.919795   9.975547   2.351259 1.000000 0.078000
14   0.000000  11.083941   3.135012 1.000000 0.078000
14   0.000000  11.083941   5.486271 1.000000 0.078000
14   3.839590   0.000000   0.000000 1.000000 0.078000
14   1.919795   3.325182   0.000000 1.000000 0.078000
14   5.759385   3.325182   0.000000 1.000000 0.078000
14   3.839590   0.000000   2.351259 1.000000 0.078000
14   1.919795   3.325182   2.351259 1.000000 0.078000
14   5.759385   3.325182   2.351259 1.000000 0.078000
14   3.839590   6.650365   0.000000 1.000000 0.078000
14   3.839590   4.433576   3.135012 1.000000 0.078000
14   1.919795   7.758759   3.135012 1.000000 0.078000
14   5.759385   7.758759   3.135012 1.000000 0.078000
14   3.839590   6.650365   2.351259 1.000000 0.078000
14   3.839590   4.433576   5.486271 1.000000 0.078000
14   1.919795   7.758759   5.486271 1.000000 0.078000
14   5.759385   7.758759   5.486271 1.000000 0.078000
14   3.839590  11.083941   3.135012 1.000000 0.078000
14   3.839590   8.867153   6.270024 1.000000 0.078000
14   1.919795  12.192335   6.270024 1.000000 0.078000
14   5.759385  12.192335   6.270024 1.000000 0.078000
14   3.839590  11.083941   5.486271 1.000000 0.078000
14   3.839590   8.867153   8.621283 1.000000 0.078000
14   1.919795  12.192335   8.621283 1.000000 0.078000
14   5.759385  12.192335   8.621283 1.000000 0.078000
14   5.759385   1.108394   3.135012 1.000000 0.078000
14   5.759385   1.108394   5.486271 1.000000 0.078000
14   5.759385   5.541971   6.270024 1.000000 0.078000
14   5.759385   5.541971   8.621283 1.000000 0.078000
14   0.000000   0.000000   0.000000 1.000000 0.078000
14   1.919795   1.108394   3.135012 1.000000 0.078000
14  -0.000000   0.000000   2.351259 1.000000 0.078000
14   1.919795   1.108394   5.486271 1.000000 0.078000
14   0.000000   4.433576   3.135012 1.000000 0.078000
14   0.000000   2.216788   6.270024 1.000000 0.078000
14   1.919795   5.541971   6.270024 1.000000 0.078000
14   0.000000   4.433576   5.486271 1.000000 0.078000
```

```
14   0.000000   2.216788   8.621283 1.000000 0.078000
14   1.919795   5.541971   8.621283 1.000000 0.078000
14   0.000000   8.867153   6.270024 1.000000 0.078000
14   0.000000   8.867153   8.621283 1.000000 0.078000
14   3.839590   2.216788   6.270024 1.000000 0.078000
14   3.839590   2.216788   8.621283 1.000000 0.078000
-1
```

Bibliography

[1] Axel Rother, Kurt Scheerschmidt. Relativistic effects in elastic scattering of electrons in tem. *Ultramicroscopy*, 109:154–160, 2009.

[2] Cowley, J. M. and Moodie, A. F. The scattering of electrons by atoms and crystals. i. a new theoretical approach. *Acta Cryst.*, 10(10):609–619, Oct 1957.

[3] D. Van Dyck. Image calculations in high-resolution electron microscopy: Problems, progress, and prospects. volume 65 of *Advances in Electronics and Electron Physics*, pages 295 – 355. Academic Press, 1985.

[4] Earl J. Kirkland. *Advanced Computing in Electron Microscopy.* Plenum Press, New York, 1998.

[5] L. M. Peng, G. Ren, S. L. Dudarev and M. J. Whelan. Robust parameterization of elastic and absorpative electron atomic scattering factors. *Acta Cryst.*, A(52):257–276, 1996.

[6] N. Zettili. *Quantum Mechanics: Concepts and Applications*. John Wiley Sons Ltd, 2nd edition, 2009.

[7] P.A. Doyle and P.S. Turner. Relativistic hartree-fock x-ray and electron scattering factors. *Acta Cryst.*, A(24):390, 1968.

[8] William H. Press, Brian P. Flannery, Saul A. Teukolsky and William T. Vetterling. *Numerical Recipes in C.* Cambridge University Press, 1988.